

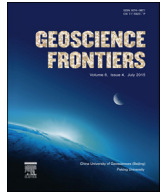
HOSTED BY



Contents lists available at ScienceDirect

China University of Geosciences (Beijing)

Geoscience Frontiers

journal homepage: [www.elsevier.com/locate/gsf](http://www.elsevier.com/locate/gsf)

Research paper

# Tectonic juxtaposition of crust and continental growth during orogenesis: Example from the Rengali Province, eastern India

Sankar Bose<sup>a,\*</sup>, Susmita Guha<sup>a</sup>, Gautam Ghosh<sup>a</sup>, Kaushik Das<sup>b</sup>, Joydip Mukhopadhyay<sup>a,c</sup><sup>a</sup> Department of Geology, Presidency University, Kolkata 700073, India<sup>b</sup> Department of Earth and Planetary Systems Science, Hiroshima University, Higashi Hiroshima, Japan<sup>c</sup> PPM Research Group, Department of Geology, University of Johannesburg, Johannesburg, South Africa

## ARTICLE INFO

## Article history:

Received 14 February 2014

Received in revised form

10 September 2014

Accepted 22 September 2014

Available online 18 October 2014

## Keywords:

Singhbhum craton

Rengali Province

Granulite enclave

Tectonic juxtaposition

## ABSTRACT

The southern boundary of the Singhbhum Craton witnessed multiple orogenies that juxtaposed thin slice of granulite suite of the Rengali Province against the low-grade granite-greenstone belt of the craton along the E–W trending Sukinda Thrust. The strong southerly dipping mylonitic foliation within the granulites along with the prominent down-dip mineral lineation, suggest a northerly-verging thrusting. Mylonitized charnockite at the contact zone contains enclaves of mafic and ultramafic granulite, whereas granitoid gneiss contains enclaves of pelitic granulite. Mafic granulite enclaves preserve an early ( $S_{1M}$ ) foliation that formed during  $D_{1M}$  deformation. This rock, along with the host charnockite, were intensely deformed by the  $D_{2M}$  thrusting event and resulting  $S_{2M}$  foliation development in both rock suites. Geothermobarometric and pseudosection analyses show that the garnet-clinopyroxene-plagioclase-orthopyroxene-ilmenite-quartz assemblage in mafic granulite was stabilized at high-pressure and temperature conditions (10–12 kbar, 860 °C) and was overprinted by a fine-grained assemblage of clinopyroxene-plagioclase ± hornblende that developed during decompression (down to 5.5–7.5 kbar). Matrix hornblende shows incipient breakdown to garnet-clinopyroxene-quartz intergrowth due to a granulite facies reworking. A contrasting  $P$ - $T$  history is preserved in the pelitic granulite. The peak assemblage garnet-orthopyroxene-cordierite-quartz-rutile was stabilized at ~6.0 kbar, 730 °C which resulted from heating of the mid crust magma during the  $D_{2M}$  thrusting. The contrasting  $P$ - $T$  histories could result from the tectonic juxtaposition of lower- and mid-crustal section during the  $D_{2M}$  event. Evidences of an early orogenic imprint within the mafic granulite imply involvement of deep continental crust during southward growth of the Singhbhum Craton.

© 2014, China University of Geosciences (Beijing) and Peking University. Production and hosting by Elsevier B.V. This is an open access article under the CC BY-NC-ND license (<http://creativecommons.org/licenses/by-nc-nd/3.0/>).

## 1. Introduction

Craton margin mobile belts, displaying complex tectonothermal histories, are the most crucial elements for understanding the growth of continents. Many ancient mobile belts evolved through multiple orogenies with several phases of deformation and metamorphism before eventual cratonization (Ennih and Liégeois, 2008; St-Onge et al., 2009). Although modern-style plate tectonics leading to continental growth argued to have existed since the Mesozoic time (Cawood et al., 2006; Dewey, 2007; Smithies et al., 2007; Condie and Kröner, 2008; Windley and Garde, 2009; Polat

et al., 2011; Samuel et al., 2014), Precambrian continental growth patterns are often blurred by the lack of a complete rock record, multiple episodes of reworking, and fragmentation and amalgamation over time (Möller et al., 1995; Stern, 2005). Despite such limitations, Precambrian craton-mobile belt “couplets” provide the best indications of early continental growth processes (Karlstrom et al., 2001; Gray and Foster, 2004; Cawood, 2005; Condie, 2007; Kröner et al., 2008). Orogenic process causes large-scale movements, particularly in the deep to mid-crustal level, resulting juxtaposition of widely varying crustal sections (Faak et al., 2012).

Peninsular India contains a mosaic of such Precambrian craton-mobile belt couplets. The Singhbhum Craton (SC) (Fig. 1a) records a remarkable Archean growth history (Saha, 1994). Its southern margin is composed of high-grade granulites along with medium-grade metasedimentary and metavolcanic rocks, collectively termed as the Rengali Province (Crowe et al., 2001, 2003; Dobmeier

\* Corresponding author.

E-mail address: [sankar.bose@gmail.com](mailto:sankar.bose@gmail.com) (S. Bose).

Peer-review under responsibility of China University of Geosciences (Beijing).

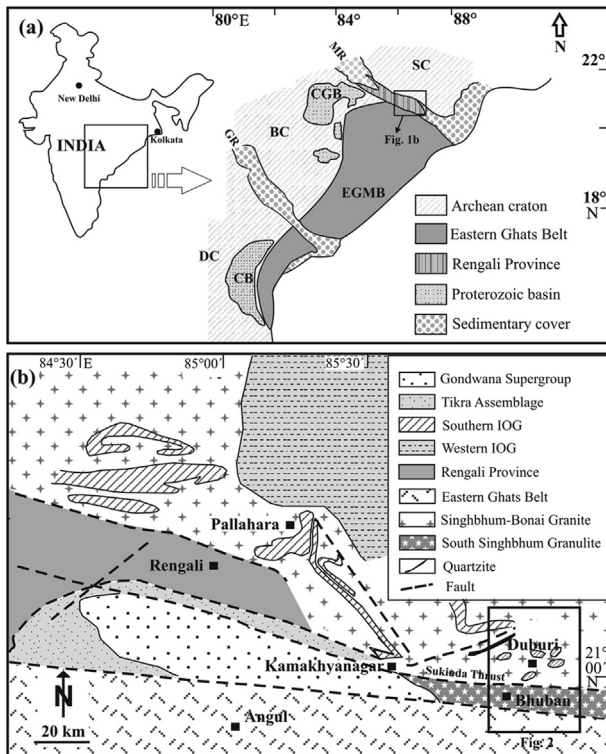


**Figure 1.** (a) Map showing positions of the Proterozoic Eastern Ghats Mobile Belt (EGMB) and Archean Singbhum Craton (SC). Other abbreviations used are: DC – Dharwar Craton, BC – Bastar Craton, MR – Mahanadi Rift, GR – Godavari Rift, CGB – Chhattisgarh Basin, and CB – Cuddapah Basin. (b) Geological map of the southern margin of the Singbhum Craton (modified after Mahalik, 1994).

and Raith, 2003) that separate the Paleo–Mesoproterozoic granite-greenstone terrane of the SC (e.g., Saha, 1994; Mukhopadhyay et al., 2012) from the essentially high-grade Paleo–Mesoproterozoic Eastern Ghats Mobile Belt (EGMB) (Bose et al., 2011; Das et al., 2011; Korhonen et al., 2011; Gupta, 2012; Dasgupta et al., 2013 and references therein). Although the Rengali Province constitutes a part of the EGMB, its rock types, metamorphic style and isotopic signatures are different from the major part of the EGMB, known as the Eastern Ghats Province or EGP (Dobmeier and Raith, 2003). In this paper, we investigate the evolution of the granulite enclaves of the eastern part of the Rengali Province to trace the complexity of the orogenic history.

## 2. Geological background

Singbhum Craton includes granite-greenstone terranes and supracrustal metasedimentary and metavolcanic successions (reviewed in Saha, 1994; Mukhopadhyay, 2001; Misra, 2006). Its southern margin is constituted of bimodal volcanics-ultramafics and a BIF-bearing greenstone succession of the southern Iron Ore Group (SIOG). The high-grade rocks along the margin of SC belong to the easternmost part of the wedge-shaped Rengali Province (Fig. 1). The Rengali granulites comprise a dominantly granitoid-charnockite rock suite with frequent mafic and pelitic granulite enclaves. The narrow strip of granulites (approx. 15 km wide) in the study area extends from the south bank of the Brahmani River up to Charaidhara in the south, beyond which it is juxtaposed with another high-grade rock suite, comprising khondalite-charnockite-augen gneiss-quartzite, of the EGP (Fig. 2).

Several granitoid bodies, intrusive in both within SIOG supracrustals and the Rengali granulite suite (Misra et al., 2000) outcrop

sporadically across the Sukinda Thrust (Fig. 2). These granitoid bodies, occurring along the hanging-wall block of the Sukinda Thrust, appear strongly foliated, sheared, and mylonitized (Fig. 3a). Moving southward from the thrust zone, thin slivers of intrusive granites occur along listric fractures within the granulites of the Rengali Province. Strain within intrusive granites visibly waned as the appearance of the rocks progressively changes from a fine-grained mylonite at or near the Sukinda Thrust to an augen gneiss (Fig. 3b) in the south. In the north of the contact zone (i.e., in the foot-wall side of the Sukinda Thrust), the intrusive granite within the cratonic rock is visibly less deformed and retains its original porphyritic character (Fig. 3c) with signs of moderate deformation and local development of a weak foliation.

Charnockitic gneisses of Rengali granulite suite contain layers and lenses of mafic granulite and ultramafic granulite, whereas pelitic granulite enclaves are present within the granitoid gneiss. Mafic granulite enclaves are extremely stretched within the charnockite mylonite near the contact zone (Fig. 3a). Some of the mafic granulite bodies are a few meters long, and centimeter-sized mafic granulite pods are also found within the host rocks. The former rock is fine- to medium-grained, dark-colored and mostly enriched in garnet and pyroxene grains. Some of the rocks contain abundant hornblende of slightly coarser size. Granitic veins occasionally cut through the mafic granulite enclaves (Fig. 3d); layers of mafic granulite occur within the charnockite suite as well. Such bands are of variable thickness (2–20 cm), and the host rock resembles a stromatic migmatite. Thick and laterally persistent mafic granulite layers show tight isoclinal folding (Fig. 3e). Felsic dikes intrude the charnockite (Fig. 3f). Pelitic granulite occurs as meter-sized enclaves within the granitoid gneiss west of the Bhuban area (Fig. 2). The rock is medium-grained with abundant garnet grains. Both the enclaves and the host gneiss are deformed, with development of pervasive foliation (Fig. 3g). Ultramafic granulite is sporadic and found as a 100 m-sized body near Bhuban (Fig. 2). The rock is dark with centimeter-sized megacrysts of orthopyroxene grains (Fig. 3h), giving it a spotted appearance.

## 3. Structural imprints

The most pervasive planar fabric within the Rengali granulite suite is the  $S_{2M}$  shear foliation. The primary  $S_{1M}$  foliation is commonly indistinguishable from  $S_{2M}$ , but locally shows folding and gets transposed by the  $S_{2M}$  shear planes (Fig. 4a). Attitude of the  $S_{1M}$  foliation varies due to large asymmetric northerly verging  $F_{2M}$  folds. Stretched gneissic layering ( $S_{1M}$ ) on limbs of  $F_{2M}$  folds within charnockite shows asymmetric boudins. The sense of movement from asymmetric folds and boudins is invariably top-to-the north/northeast on southerly dipping shear planes. Granite veins are emplaced synkinematically along listric fractures parallel to or at low angles with the  $S_{2M}$  shear planes (Fig. 4b). These granite bodies often preserve well-developed S-C structures consistent with the top-to-the-north shear sense.

The penetrative foliation within the charnockite mylonite ( $S_{CH}$ ) is defined by orthopyroxene + garnet-rich mafic and quartz + feldspar-rich felsic layers and parallels the contact with the cratonic rock suite. The felsic layers invariably show stretched feldspar crystals with effects of widespread dynamic recrystallization in the form of core-mantle structures (Fig. 4c). Quartz grains, on the other hand, are totally recrystallized to form a strain-free fine-grained equigranular mosaic leaving few quartz ribbon relicts (Fig. 4d). This  $S_{CH}$  is actually a composite shear-related fabric often comprising of S-C structures. Elongated and fractured garnet grains locally develop asymmetric recrystallized tails (Fig. 4e) that, together with the S-C structures observed in outcrop-scale, point toward a consistent top-to-the-north up-dip movement on a south-

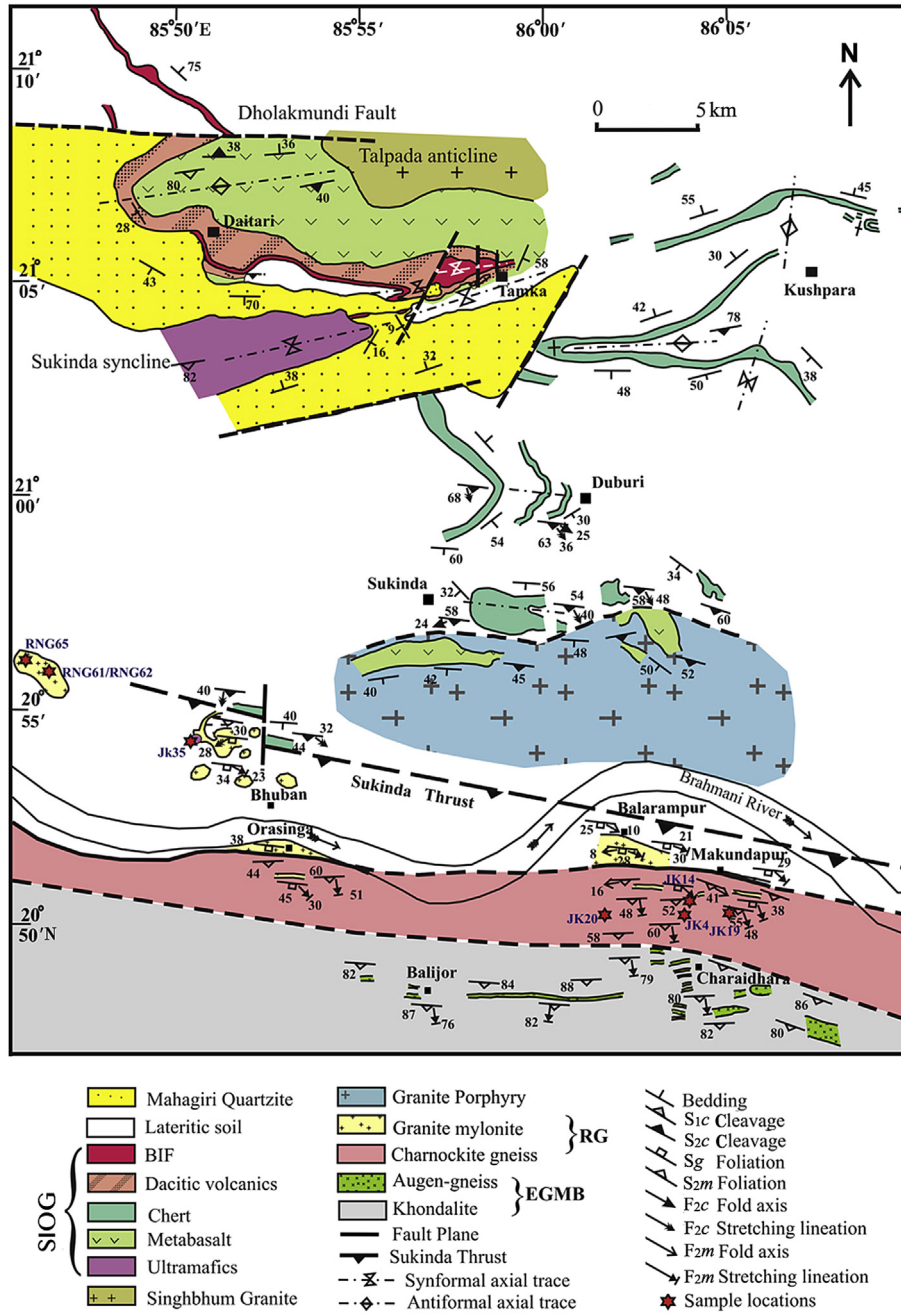


**Figure 2.** Geological map of Bhuban-Duburi-Charaidhara area showing rock types and structural features (modified after Ghosh et al., 2010; Mukhopadhyay et al., 2012). Samples used in the present study are shown in the map. RG represents Rengali granulites.

dipping foliation plane (Fig. 4f). The  $S_{2M}$  foliation in the Rengali granulite is concordant with the  $S_{CH}$  indicating the latter foliation correlates with the  $D_{2M}$  shearing event within the Rengali Province. The folded  $S_{1M}$  foliation within the enclave suite implies an earlier deformation event ( $D_{1M}$ ).

Large folds have profusely developed within the cratonic foot-wall of the Sukinda Thrust whose long drawn-out limbs show an E–W trend steeply dipping due south while short, thickened hinges plunge moderately toward the southeast or southwest. These folds are essentially non-cylindrical, inclined, and northerly-verging. Both bedding ( $S_0$ ) and an earlier schistosity ( $S_{1C}$ ) in chert are folded (Fig. 4g), with development of an axial planar  $S_{2C}$  fabric that trends E–W and dips moderately due south. The concordance of  $S_{2C}$  with both  $S_{CH}$  and  $S_{2M}$  foliations indicates

that the dominant  $D_{2M}$  shearing deformation in the granulite suite was responsible for deformation in the cratonic rocks ( $D_{2C}$ ) and the charnockite along the contact. The asymmetry and northward vergence of the  $F_{2C}$  folds indicate a top-to-the-north shear, consistent with a similar kinematic pattern in the overlying charnockite mylonite, occurring in the hanging-wall of the Sukinda Thrust.

#### 4. Metamorphic imprints on the granulite enclaves

##### 4.1. Textural and mineralogical evolution

Mafic granulite is medium- to coarse-grained and composed of clinopyroxene, garnet, quartz, plagioclase, ilmenite and hornblende



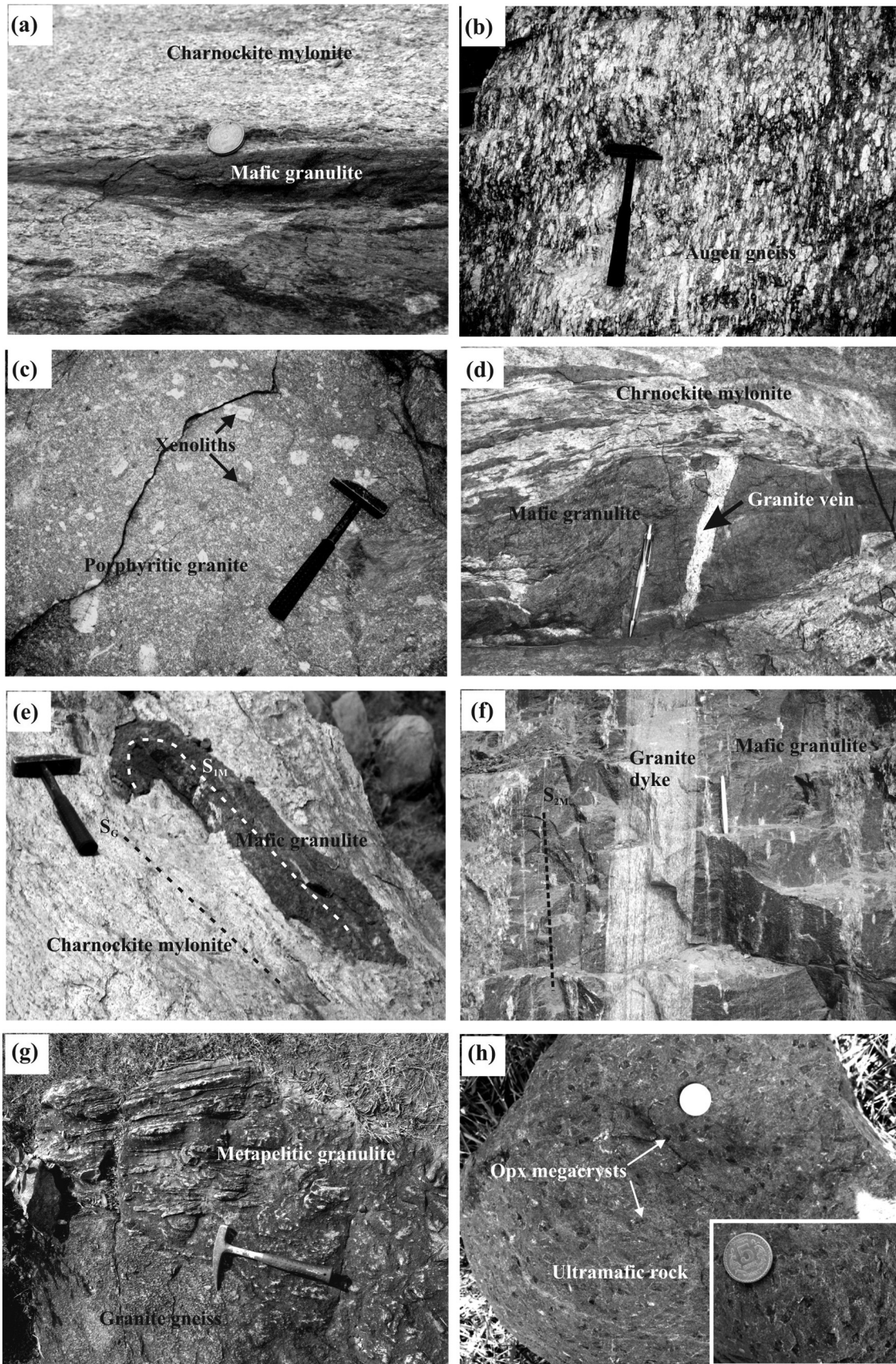
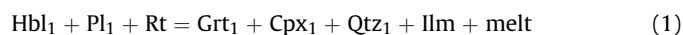


**Figure 3.** Field photographs showing features of the RG, EGMB and SC rocks. (a) Mafic granulite enclave within the charnockite mylonite of RG. (b) Augen gneiss of probable EGMB lineage exposed at the southern part of study area. (c) Porphyritic granite within SC showing xenoliths of SIOG rocks. (d) Granite vein cuts through mafic granulite enclave within charnockite mylonite of Rengali suite. (e) Folded mafic granulite enclave within RG charnockite mylonite shows early  $S_{1M}$  foliation. (f) Granite dyke cuts through mafic granulite of RG suite along  $S_{2M}$  foliation. Note the presence of alkali feldspar augen along the steep  $S_{2M}$  plane. (g) Metapelitic granulite occurring as enclave within granite gneiss. Note the strong foliation developed in the former. (h) Spotted ultramafic granulite showing orthopyroxene megacrysts. Inset shows very fine collar of plagioclase surrounding the orthopyroxene megacrysts.



with subordinate amount of orthopyroxene, rutile and magnetite. The peak granulite assemblage is represented by garnet-clinopyroxene-plagioclase-quartz-ilmenite with/without orthopyroxene which is characteristic of many high-pressure rocks (O'Brien, 2008; Racek et al., 2008). This assemblage could have evolved through dehydration melting of hornblende-bearing assemblage. Tiny rounded inclusions of hornblende within garnet (Fig. 5a) suggest a possible reaction (Eq. 1):



In this reaction, Hbl<sub>1</sub> represents relict hornblende whereas Grt<sub>1</sub>, Cpx<sub>1</sub> and Qtz<sub>1</sub> represent peak phases. Presence of thin films and patches of quartz surrounding plagioclase (Fig. 5b), cusped grain boundaries of quartz and plagioclase surrounding garnet and clinopyroxene grains, and local development of euhedral faces of garnet against quartzofeldspathic aggregate collectively suggest possible involvement of melt phase (Sawyer, 1999; Brown, 2002). Experimental data on hornblende dehydration melting show the stability of the restite assemblage of garnet + clinopyroxene + quartz ± Fe–Ti oxides form at pressure > 10 kbar (Skjerlie and Patinõ Douce, 1995) with tonalitic to trondhjemitic melt composition (Beard and Lofgren, 1991; Rushmer, 1991, 1993; Wolf and Wyllie, 1994; Springer and Seck, 1997).

Garnet porphyroblasts are commonly surrounded by a recrystallized intergrowth of clinopyroxene + plagioclase ± hornblende (Fig. 5c). This texture is different from the reported symplectic intergrowth after garnet from many high-pressure granulites (Pitra et al., 2010; Faak et al., 2012).

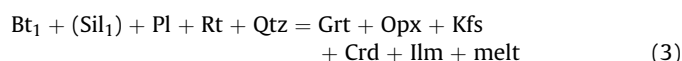
All the porphyroblastic phases are extremely deformed and stretched along the foliation (Fig. 5d). A coarse intergrowth of garnet-clinopyroxene-quartz forms clusters (Fig. 5e). Bipartite grains of ilmenite-magnetite exist within the spongy intergrowth (Fig. 5f). Most of the garnet grains are spindle-shaped and show stretching along the foliation (Fig. 5g), but a few idioblastic garnet grains are also present within the quartz-plagioclase leucosome (Fig. 5h). The garnet breakdown reaction can be explained by the following reaction:



Presence of tiny grains of hornblende in the intergrowth may imply hornblende was produced directly in the garnet breakdown reaction in which case, the presence of melt is required. On the other hand, hornblende can form in a separate process much later during hydration and retrogression.

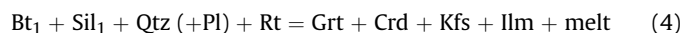
Intrusion of granite along the foliation is common feature of the mafic granulite. Rafts and stringers of clinopyroxene grains are present in the granite layers within which quartz, perthite and plagioclase grains are extremely stretched to exhibit a mylonite fabric (Fig. 5i). Secondary hornblende replacing the garnet and clinopyroxene grains demarcates the retrogressive change within the mafic granulites. Although some of the hornblende crystals show static recrystallization, most form tiny stretched grains along with the clinopyroxene-plagioclase intergrowth (Fig. 5j). This hornblende-clinopyroxene-plagioclase intergrowth occurs as an anastomosing micro-shear fabric. Coarse hornblende grains (peak?) in sample RNG 65A show marginal breakdown to a fine spongy intergrowth of garnet-quartz ± clinopyroxene (Fig. 5k). Such intergrowth also invades the hornblende grain interior. Garnet grain in such intergrowth is very fine and euhedral in outline (Fig. 5l). It implies a granulite-grade reworking of the retrogressed granulite through reaction (Eq. 1). Owing to the restricted occurrence of the product phases, the reaction appears to be incipient in nature.

Pelitic granulites are composed of garnet, sillimanite, rutile, ilmenite, cordierite, quartz, K-feldspar (perthite) and variable amounts of plagioclase and biotite. Orthopyroxene occurs as clusters with garnet in one sample (RNG 62b) and is surrounded by quartzofeldspathic matrix (Fig. 6a). Plagioclase is present in this association. Garnet grains in such clusters show intergrowth with vermicular quartz in the peripheral part (Fig. 6b). The garnet-quartz intergrowth overgrows the coarse garnet (Fig. 6c). Garnet crystals share stable grain contact with cordierite and contain inclusions of randomly oriented fibrous sillimanite and tiny elliptical biotite (Fig. 6d). Orthopyroxene, cordierite, plagioclase, ilmenite and quartz show evidence of deformation. Rutile grains occur both within garnet and in the quartzofeldspathic matrix. Presence of thin films of alkali feldspar over quartz and plagioclase grains, cusped nature of quartz and feldspar grains and biotite-rich selvage surrounding leucocratic layers (Fig. 6e) suggest possible involvement of melt phase during the peak metamorphism. These features imply that the peak metamorphic assemblage of garnet + cordierite + orthopyroxene + quartz + K-feldspar + ilmenite was formed after dehydration melting of biotite + sillimanite + plagioclase-bearing protolith through



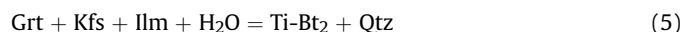
Here Bt<sub>1</sub> and Sil<sub>1</sub> represent included phases within garnet porphyroblast.

In the orthopyroxene-free pelitic granulite (sample RNG 61B), garnet, cordierite and quartz form the medium-grained granulitic aggregate (Fig. 6f), while sillimanite needles occur both within garnet and quartz-perthite-rich matrix. The possible reaction is



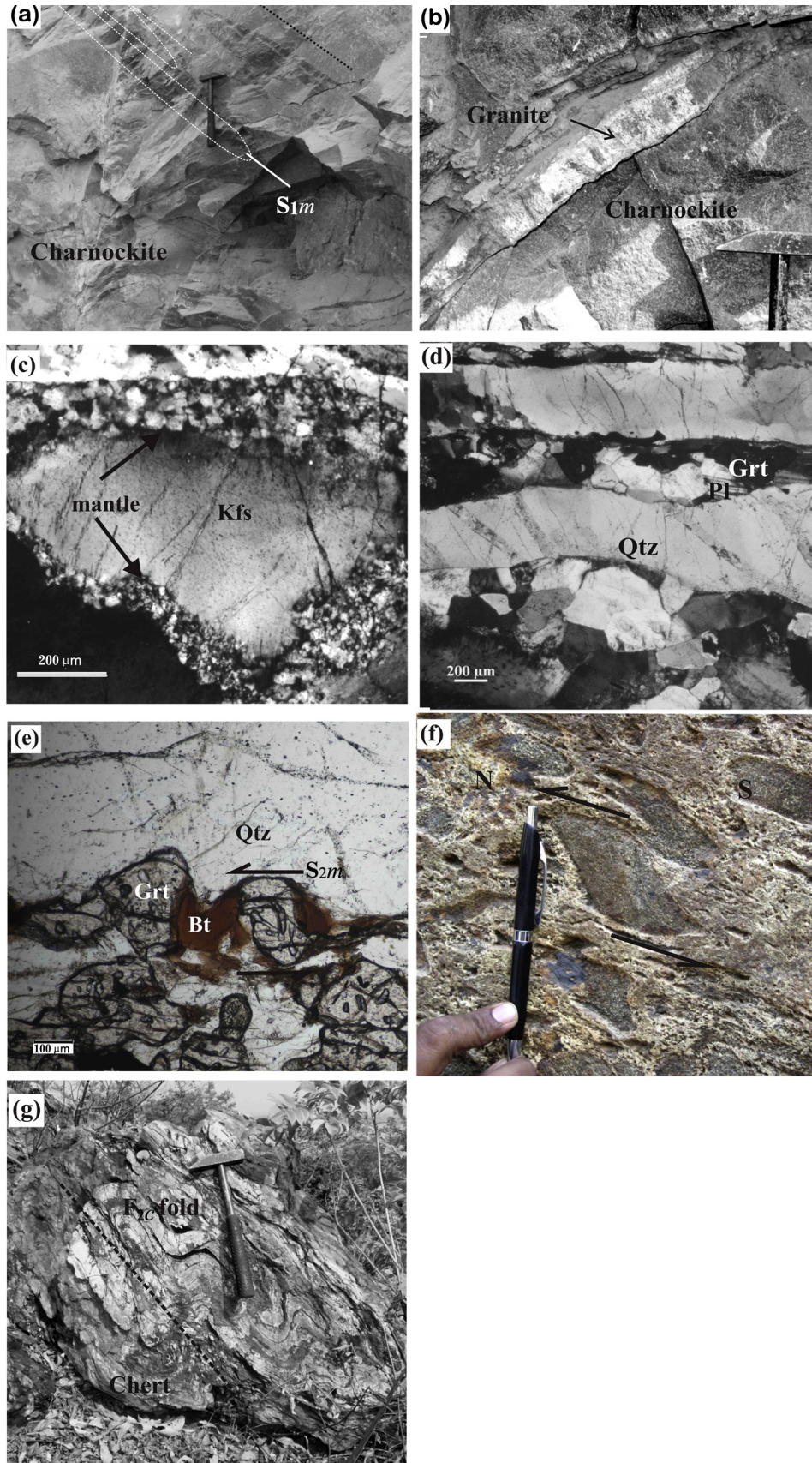
Experimental data in the pelitic system show that this melting reaction has a steep positive slope and occurs at 6.0–9.0 kbar/850 °C (Carrington and Harley, 1995).

In both the samples, garnet grains are marginally replaced by biotite and/or biotite-quartz intergrowth (Fig. 6d), which possibly occurs due to the reaction:



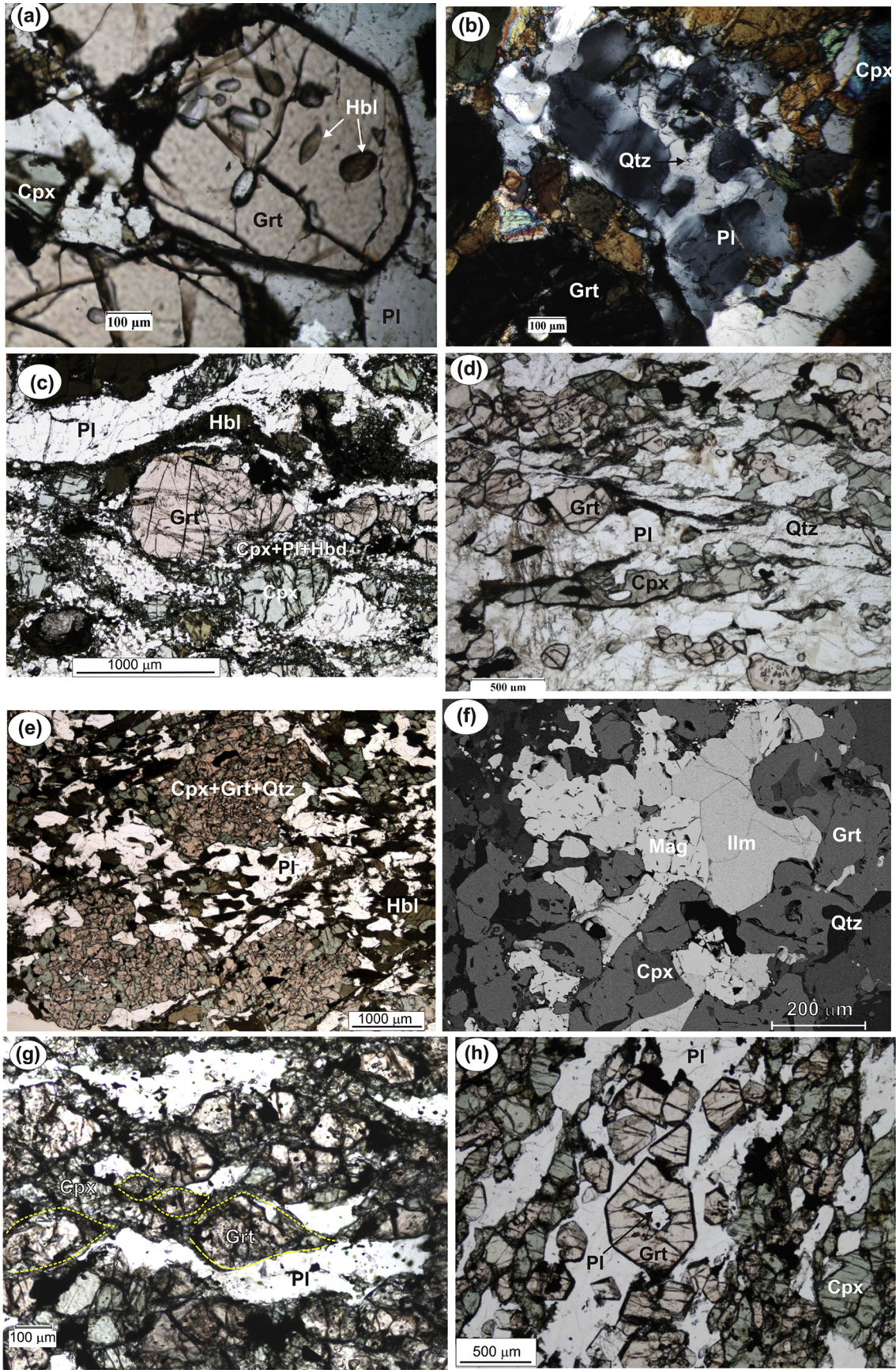
This reaction was possibly responsible for the stability of the assemblage Bt-Grt-Ilm-Qtz in the retrograde assemblage.

Ultramafic granulite is constituted of megacrystic orthopyroxene surrounded by a finer matrix of granular orthopyroxene, clinopyroxene, and locally hornblende (Fig. 6g). Backscatter electron imaging reveals tiny plagioclase lamellae along a prominent crystallographic plane of the orthopyroxene megacrysts (Fig. 6h). Plagioclase also forms a collar surrounding the megacrystic grain. Excepting minor plagioclase and hornblende, the rock is composed of pyroxene grains. All the matrix grains and the megacrysts are deformed, the former particularly showing recrystallized grain boundaries. Microshear bands are the other notable features. Mineralogical evolution of this rock centers on the development of orthopyroxene megacrysts and its exsolved products. Similar texture involving orthopyroxene is reported from anorthositic rocks (Charlier et al., 2010 and references therein). Most workers consider such orthopyroxene megacrysts as exotic, either formed under high-pressure conditions (Emslie, 1975; Charlier et al., 2010) or due to rapid growth under suitable conditions (Dymek and Gromet, 1984; Owens and Dymek, 1995). Plagioclase as an exsolved phase implies breakdown of Ca-Tschermak (CaTs) and



**Figure 4.** (a) Photograph showing tight isoclinal  $F_{2M}$  folding and transposition of  $S_{1M}$  foliation by  $S_{2M}$  in charnockite. (b) Photograph showing granitic leucosome emplaced along  $S_{2M}$ -parallel listric fractures in charnockite. (c) Photomicrograph of deformed alkali feldspar grain (Kfs) in charnockite mylonite showing 'core-mantle' structure. (d) Photomicrograph of quartz ribbons (Qtz) within charnockite mylonite. (e) Photomicrograph showing asymmetric garnet (Grt) grains having tails in charnockite mylonite. Note the presence of biotite (Bt) at the fringe of garnet. (f) Photograph showing asymmetric quartz clasts having top-to-the-north sense of shear. (g) Photograph of asymmetric  $F_{2C}$  folds disrupted by later faults (dashed line) in SIOG chert.







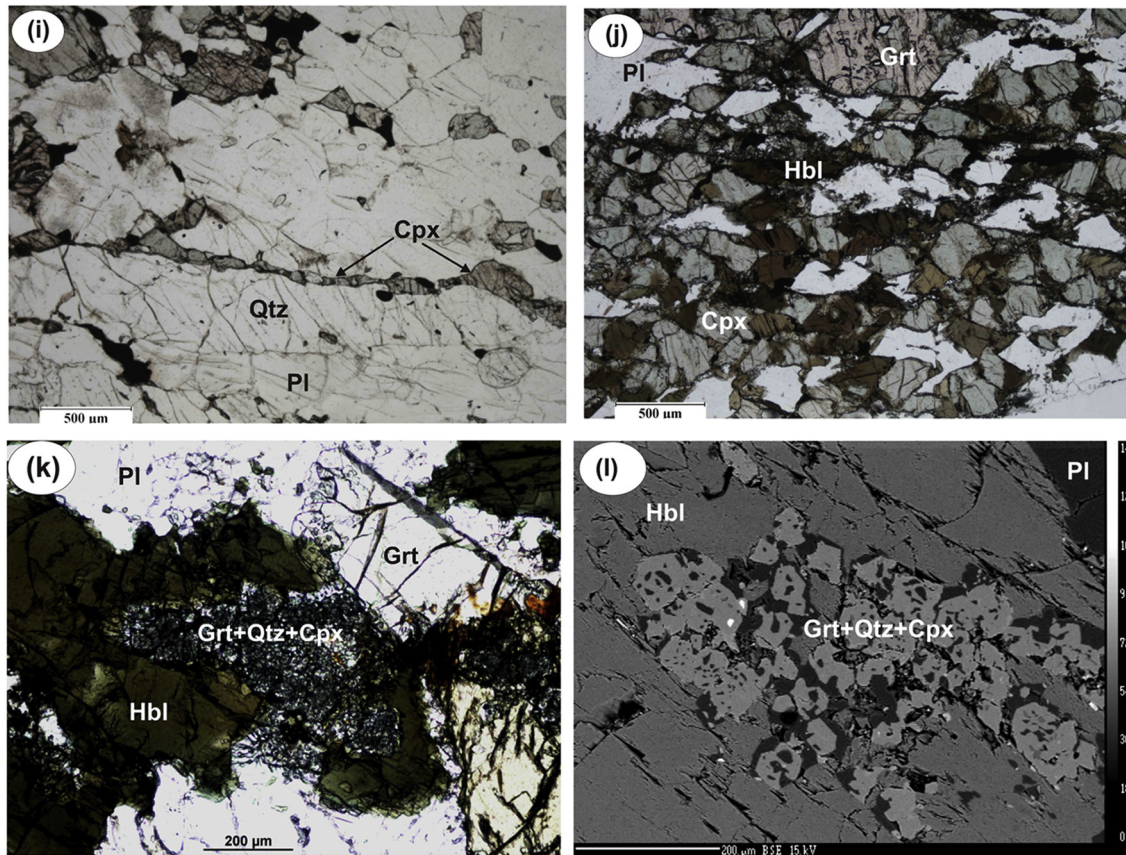
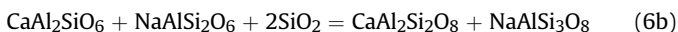
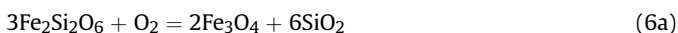


**Figure 5.** Photomicrographs and back scattered electron (BSE) images of mafic granulite. (a) Garnet (Grt) grain containing inclusion of hornblende (Hbl) in association with clinopyroxene (Cpx) and plagioclase (Pl) in sample RNG 65A. (b) Thin film of quartz (Qtz) developed surrounding plagioclase (Pl) in association of clinopyroxene (Cpx) and garnet (Grt). (c) Coarse garnet (Grt) is surrounded by fine recrystallized intergrowth of clinopyroxene + plagioclase ± hornblende (Cpx + Pl ± Hbl) in sample RNG 65A. Coarse clinopyroxene and plagioclase grains are also present in the microdomain. (d) Stretched clinopyroxene (Cpx), quartz (Qtz), plagioclase (Pl) grains in sample JK 20. (e) Coarse spongy intergrowth of garnet-clinopyroxene-quartz (Cpx + Grt + Qtz) in sample JK4B. (f) BSE image showing bipartite magnetite (Mag) and ilmenite (Ilm) grains within the garnet-clinopyroxene-quartz spongy intergrowth in sample RNG 65A. (g) Sheared spindle-shaped garnet (Grt) in association with stretched clinopyroxene (Cpx) and plagioclase (Pl) in sample JK 14B. (h) Euhedral garnet (Grt) contains inclusions of plagioclase (Pl) in sample JK14B. Coarse plagioclase and clinopyroxene (Cpx) are associated with garnet grains. (i) Extremely stretched and torn clinopyroxene (Cpx) grains showing a mylonitic foliation  $S_{1M}$  along with quartzofeldspathic layer (Qtz-Kfs-Pl) in sample JK14C. (j) Late hornblende (Hbl) replaces porphyroblastic garnet (Grt) in sample JK20. Note that the hornblende grains are stretched in nature. (k) Fine intergrowth of garnet-quartz ± clinopyroxene (Grt + Qtz ± Cpx) replaces coarse hornblende (Hbl) in the vicinity of porphyroblastic garnet in sample RNG 65A. (l) BSE image of the intergrowth showing euhedral nature of garnet in the intergrowth in sample RNG 65A.

jadeite (Jd) components that are normally present in very low amount in orthopyroxene. This is reflected in the very low modal occurrence of exsolved plagioclase. To balance such a reaction, one needs a small amount of silica in the form of quartz, which is not commonly present in an ultramafic protolith. Dymek and Gromet (1984) explained that some amount of silica can be released from conversion of the ferrosilite component of orthopyroxene to magnetite with the aid of oxygenated fluid. The actual reaction will be a combination of the following two:



Tiny ilmenite needles within orthopyroxene possibly imply a much more complicated reaction than is reported in earlier studies (Charlier et al., 2010). Such reactions occur either in the subsolidus stage during decompression (Emslie, 1975), or in the suprasolidus stage due to polybaric fractionation (Charlier et al., 2010). Experimental data on orthopyroxene megacrysts reveal that aluminous orthopyroxene (> 3 wt.%  $\text{Al}_2\text{O}_3$ ) is stable at 11–13 kbar (Fram and Longhi, 1992; Longhi et al., 1993). Plagioclase collar on

megacrystic orthopyroxene could form by granular exsolution which caused the products to come out of the host.

#### 4.2. Mineral chemistry

Representative samples were analyzed with a 4-spectrum CAMECA SX-100 Electron Microprobe at the Indian Institute of Technology, Kharagpur, India. The instrument was operated at 15 kV acceleration voltages using 15 nA specimen current. A 1- $\mu\text{m}$  probe diameter for the spot size was used for point analyses. A second set of chemical analysis was done using a 4-Spectrometer CAMECA SX-100 Electron Microprobe at the Wadia Institute of Himalayan Geology, Dehradun, India, operated with 15 kV accelerating voltage, a 1  $\mu\text{m}$  beam diameter, and a 20 nA beam current. To check consistency of results from the two different instruments, we repeated analysis of the same grains. The results remained almost identical within the uncertainty limits. Element mapping in selected garnet grains was done at the Department of Earth and Planetary Systems Science, Hiroshima University, Japan using a JEOL JXA-8200 Electron Microprobe. Tables 1–3 display representative analytical data.

Garnet grains in mafic granulite show minor compositional variation in different samples (Table 1). Pyrope and almandine show prominent variation, 16–20 mol.% and 53–63 mol.%, respectively, whereas grossular shows a more restricted (16–27 mol.%) variation. Idioblastic garnet grains show a minor increase in pyrope from core to rim ( $\Delta\text{Py} = 1$  mol.%) and a concomitant decrease in grossular from core. Stoichiometric balancing of unit formula shows presence of small amount of ferric iron (1.5–3.0 wt.%  $\text{Fe}_2\text{O}_3$ ). Spessartine components in all garnet grains are low (< 3 mol.%). Element maps of porphyroblastic garnet do not show any remarkable zoning, but profiles for Ca, Mg, Fe and Mn show minor variation. Profile of Ca shows minor rimward increase while that of Mg shows concomitant decrease (Fig. 7). Plagioclase shows a compositional variation in different samples. In sample JK4B, plagioclase is rich in albite ( $\text{Ab}_{63-66}\text{An}_{32-34}\text{Or}_{2-3}$ ), while composition is more variable ( $\text{Ab}_{60-68}\text{An}_{20-40}\text{Or}_{0-2}$ ) in sample JK8B. Clinopyroxene grains also show compositional variations in different samples in terms of  $X_{\text{Mg}}$  (0.60–0.75). Clinopyroxene grains in sample JK20 have the most magnesian ( $X_{\text{Mg}} = 0.74-0.75$ ), whereas those in sample JK4B have the least magnesian ( $X_{\text{Mg}} = 0.59-0.64$ ). All the grains contain variable Al (1.0–3.3 wt.%  $\text{Al}_2\text{O}_3$ ). Recalculated unit formula based on charge balance does not show any ferric iron in the structure. Although there is no zoning in terms of Fe and Mg, alumina zoning occurs in some coarse grains. All the grains contain small amounts of Na (1.1–1.4 wt.%  $\text{Na}_2\text{O}$ ) as a jadeite component. Orthopyroxene grains show  $X_{\text{Mg}}$  values 0.45 to 0.55, with low alumina (<1.0 wt.%). Ilmenite contains up to 1.4 wt.% MgO as geikielite. Matrix hornblende ( $X_{\text{Mg}} = 0.55-0.56$ ) contains a small amount of Ti ( $\text{TiO}_2$  up to 2.0 wt.%). Hornblende inclusions within garnet are slightly more magnesian ( $X_{\text{Mg}} = 0.51-0.52$ ) and contain slightly higher Ti ( $\text{TiO}_2 = 2.5-2.6$  wt.%). Biotite ( $X_{\text{Mg}} = 0.50-0.51$ ) contains 5–6 wt.%  $\text{TiO}_2$ . Fluorine is negligible in both biotite and hornblende (<0.3 wt.%). Magnetite is almost pure.

In mafic granulite sample RNG 65A, hornblende ( $X_{\text{Mg}} = 0.58-0.67$ ) contains 2.1–2.2 wt.%  $\text{TiO}_2$ , marginally higher compared to matrix hornblende (1.7–2.0 wt.%  $\text{TiO}_2$ ). Fluorine is low (<0.3 wt.%) in all the varieties. Garnet intergrown with quartz and clinopyroxene after matrix hornblende is compositionally uniform ( $\text{Alm}_{53-55}\text{Prp}_{18-21}\text{Gr}_{24-28}\text{Sps}_{1-2}$ ). Intergrown clinopyroxene is more magnesian ( $X_{\text{Mg}} = 0.73-0.76$ ), less aluminous ( $\text{Al}_2\text{O}_3 = 1.72-2.0$  wt.%) and low in Na ( $\text{Na}_2\text{O} < 0.8$  wt.%) compared to porphyroblastic grains ( $X_{\text{Mg}} = 0.70-0.71$ ; 3.0–3.3 wt.%  $\text{Al}_2\text{O}_3$  and ~1.0 wt.%  $\text{Na}_2\text{O}$ ). Plagioclase cores contain 56–58 mol.% albite and 41–43% anorthite components.

In the metapelitic granulite (Table 2), garnet shows compositional variation in terms of almandine-pyrope ( $\text{Prp}_{38-43}\text{Alm}_{53-58}$ ) whereas grossular and spessartine are usually minor (< 5 mol.% in total). Small quantity of ferric iron is present (0–2.3 wt.%  $\text{Fe}_2\text{O}_3$ ). Orthopyroxene shows compositional variation in terms of alumina (3.6–5.4 wt.%  $\text{Al}_2\text{O}_3$ ) and Fe/Mg ratio ( $X_{\text{Mg}} = 0.68-0.70$ ). A small amount of ferric iron is present (0–2.5 wt.%  $\text{Fe}_2\text{O}_3$ ) for stoichiometric balancing of all the orthopyroxene compositions. Biotite inclusions ( $X_{\text{Mg}} = 0.84$ ) are compositionally more magnesian compared to matrix phases ( $X_{\text{Mg}} = 0.75-0.82$ ), but distinctly Ti-poor (0.2–0.4 wt.%  $\text{TiO}_2$ ) compared to the latter (5.1–6.2 wt.%  $\text{TiO}_2$ ). F in all the grains is below 0.6 wt.%. Cordierite grains are extremely magnesian ( $X_{\text{Mg}} = 0.85-0.90$ ) and oxide totals measure 98–99 wt.% implying possible presence of small amount of volatile. Plagioclase contains 46–62 mol.% albite whereas alkali feldspar contains 10–12 mol.% albite. Plagioclase lamellae in perthite are more albitic ( $\text{An}_{18-21}\text{Ab}_{69-76}\text{Or}_{2-13}$ ). Host alkali feldspar contains up to 10 mol.% albite. Rutile is almost pure whereas sillimanite contains up to 1 wt.%  $\text{Fe}_2\text{O}_3$ .

Representative mineral compositions for the ultramafic granulite are presented in Table 3. Megacrystic orthopyroxene is more aluminous (3 wt.%  $\text{Al}_2\text{O}_3$ ) compared to the matrix orthopyroxene (< 3 wt.%  $\text{Al}_2\text{O}_3$ ). Alumina in the lamellae-free core regions are high (close to 3 wt.%) and decreases close to plagioclase lamellae (~1 wt.%). The latter composition is similar to the matrix orthopyroxene compositions. CaO (3.2 wt.%) and  $\text{Na}_2\text{O}$  (0.2 wt.%) also decrease close to the plagioclase lamellae. Recalculated formula unit shows minor but variable ferric iron contents (0–1.4 wt.%  $\text{Fe}_2\text{O}_3$ ). Plagioclase lamellae have a uniform composition of  $\text{Ab}_{48}\text{An}_{51-52}\text{Or}_1$ , almost identical to the plagioclase composition in the collar surrounding megacrystic orthopyroxene. Clinopyroxene is slightly aluminous (1.5–2.0 wt.%  $\text{Al}_2\text{O}_3$ ) and magnesian in nature ( $X_{\text{Mg}} = 0.72-0.73$ ). All the grains contain insignificant amounts of  $\text{Na}_2\text{O}$  (0–0.23 wt.%). Ferric iron content is very low (0–0.9 wt.%  $\text{Fe}_2\text{O}_3$ ).

#### 4.3. Geothermobarometry

Conventional thermobarometric estimation of the studied samples was done using mineral assemblages equilibrated under different stages of metamorphic history. The results vary within estimated range even for a particular stage as reported in Table 4.

Peak *P-T* conditions for the mafic granulites were estimated using the assemblage clinopyroxene-plagioclase-garnet-quartz in different samples. For each sample, we calculated *P-T* values using point chemical data of coexisting phases from more than one microdomain. The estimates vary in the window of 712–860 °C, 11.0–12.2 kbar in different samples (Table 4). Temperature values estimated using garnet-clinopyroxene thermometer range 800–860 °C for core compositions, while rim compositions yield lower values (<800 °C). The garnet-clinopyroxene-plagioclase-quartz assemblage present in many mafic granulite samples yield pressure in the range 11.0–12.2 kbar. Maximum pressure is calculated as 12.2 kbar from the sample JK 19B, Sample RNG 65A, which preserves maximum textural features for peak  $M_1$  metamorphism, yields 11.0–11.5 kbar pressure. In the ultramafic granulite (sample JK 35), conventional barometric estimation is fraught with difficulty owing to limited choice of models. Megacrystic orthopyroxene with > 3 wt.% alumina must have crystallized at a pressure of 11.0 kbar as suggested by experimental data (Longhi et al., 1993). This should be taken as minimum estimate since the measured alumina content is leftover after exsolution of plagioclase. The matrix clinopyroxene-plagioclase assemblage gives 9.5–10.0 kbar pressure using the CaTs-An barometer of McCarthy and Patino Douce (1998). The coexisting pyroxene pairs give temperatures 772–831 °C.

*P-T* conditions during the post-peak metamorphic stage ( $M_{1R}$ ) were estimated using the hornblende-bearing assemblage in mafic granulite. The estimated *P-T* window is 624–790 °C, 5.5–7.5 kbar. The hornblende-plagioclase pair gives higher temperatures (760–790 °C at 6 kbar) compared to the hornblende-garnet thermometer (624–724 °C). The hornblende Al-barometer gives 5.5–7.5 kbar at 700 °C in different samples. This upper bracket of pressure is similar to the estimates we got using the garnet-hornblende barometer from the same samples (6.9–7.5 kbar). Hornblende compositions with moderate to low Al yield 5.0–5.5 kbar pressure.

In the metapelitic granulite, the assemblage garnet-orthopyroxene-plagioclase-quartz in sample RNG 62b was used to estimate the *P-T* conditions of peak- $M_2$  stage (Table 4). The garnet-orthopyroxene thermometer results show a temperature range of 690–731 °C at an assumed pressure of 6.0 kbar. The garnet-orthopyroxene-plagioclase-quartz barometer gives pressure of 5.7 kbar at an assumed temperature of 800 °C. The garnet-orthopyroxene-plagioclase-quartz thermobarometry using the



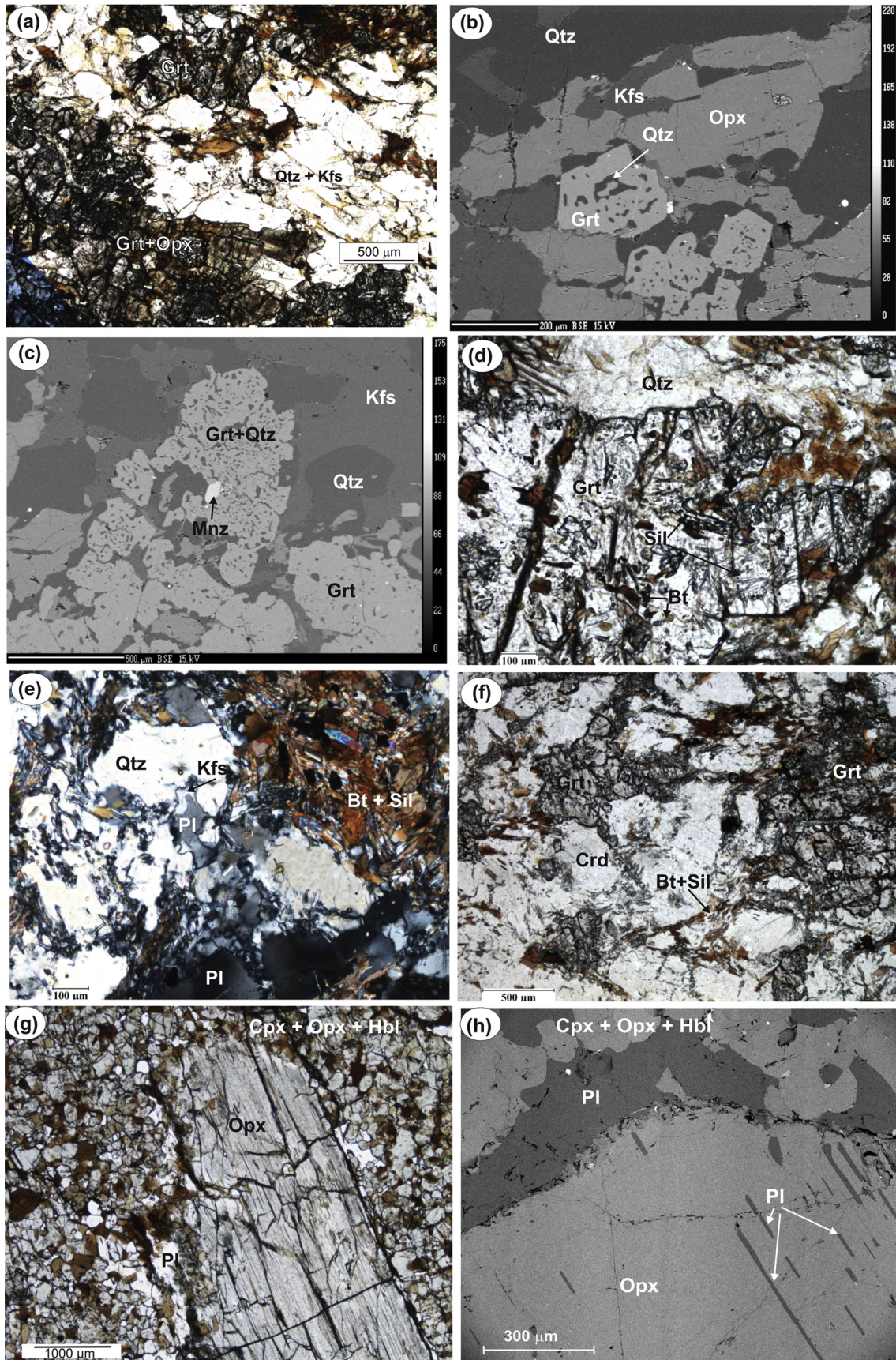


**Figure 6.** Photomicrographs and back scattered electron (BSE) images of pelitic and ultramafic granulite. (a) Gneissic layering is shown by the Garnet (Grt)-orthopyroxene (Opx) layer alternating with quartzfeldspathic layer (Qtz + Kfs) in pelitic granulite sample RNG 62b. (b) BSE image of the garnet (Grt)-orthopyroxene (Opx) layer of the same sample



convergence method of Pattison et al. (2003) yields 5.8 kbar and 679 °C temperature. The garnet-cordierite thermometer gives much lower temperature of 583–598 °C at an assumed pressure of 6 kbar. The garnet-cordierite barometer gives pressure estimates of 4.1–4.3 kbar that are lower compared to the garnet-orthopyroxene assemblage. The garnet-biotite pair gives 522–594 °C temperature which can be considered as the temperatures during  $M_{2R}$  stage.

In summary, the peak metamorphic stage in the mafic and the ultramafic granulite was attained at ~10.0–12.0 kbar pressures, 860 °C ( $M_1$ ). The rock was later retrogressed down to a  $P$ - $T$  window of 5.5–7.7 kbar, 620–790 °C ( $M_{1R}$ ). This implies a significant drop in pressure ( $\Delta P = 4.0$ – $6.0$  kbar) with moderate cooling ( $\Delta T = 100$ – $200$  °C). The granulite-grade reworking took place roughly at this stage ( $M_2$ ). The metapelitic granulite shows a contrasting  $P$ - $T$  history. The peak metamorphic condition is reached at ~6.0 kbar, 580–730 °C ( $M_2$ ). The post-peak stage witnessed retrogression of the pelitic granulite down to 500–600 °C, 4.0–4.5 kbar ( $M_{2R}$ ) pressure recorded from the biotite and cordierite-bearing assemblages.

#### 4.4. Pseudosection analysis

Metamorphic evolution of the studied granulites was further investigated using calculated  $P$ - $T$  pseudosections. Such analysis not only yields quantitative  $P$ - $T$  estimations, but also allows the investigation and understanding of the paragenetic evolution of the rocks. We adopted two different chemical systems with suitable bulk compositions for mafic and pelitic granulites.

Phase relations of the mafic granulites were modeled in the chemical system  $\text{Na}_2\text{O}$ - $\text{CaO}$ - $\text{FeO}$ - $\text{MgO}$ - $\text{Al}_2\text{O}_3$ - $\text{SiO}_2$ - $\text{H}_2\text{O}$ - $\text{TiO}_2$ - $\text{MnO}$  (NCFMASHTMn) using the program PERPLEX (Connolly and Pettrini, 2002; version 07). We chose not to include  $\text{Fe}_2\text{O}_3$  as a variable since presence of  $\text{Fe}^{3+}$  in ferromagnesian phases is minor. These phase diagrams are calculated as functions of pressure and temperature using the technique of free energy minimization (Connolly, 2005). The database file was used after Holland and Powell (1998) while the solut08.dat file was run for constraining the solution properties of phases. Activity models used are garnet (Holland and Powell, 1998), clin amphibole (Dale et al., 2005), clinopyroxene (Holland and Powell, 1998), orthopyroxene (Holland and Powell, 2003) and plagioclase (Newton et al., 1980). Rutile and ilmenite are considered as pure phases. There is no appropriate melt model for metabasic systems. We considered that the assemblages on the high-temperature side of the pseudosections may be metastable with respect to assemblages involving melt, or at least coexist with melt. However, experimental work, calculations and natural observations suggest that the topology of the phase relationships is similar when mineral assemblages coexist with fluid ( $\text{H}_2\text{O}$ ) or melt and that the field boundaries may not move significantly (e.g. Wolf and Wyllie, 1994; Vielzeuf and Schmidt, 2001; Pattison, 2003).  $P$ - $T$  pseudosections were calculated and contoured with compositions of key solid solution phases in order to bracket the conditions of peak metamorphic events within the broad stability fields of high-variance assemblages. Although the studied mafic granulite shows stability of various mineral assemblages in different

samples, we chose one representative sample (RNG 65A) for pseudosection analyses because this provides the unequivocal evidence of peak metamorphic history. The bulk rock composition used in the calculations was obtained from the whole rock XRF data (Table 5). The resultant section (Fig. 8a) shows that the stability field of the peak  $M_1$  assemblage in mafic granulite ( $\text{Grt} + \text{Pl} + \text{Cpx} + \text{Ilm} + \text{Qtz} \pm \text{Opx}$ ) is too large to constrain the peak  $P$ - $T$  conditions. Therefore, we mark the peak  $M_1$  condition in Fig. 8b on the basis of positions of calculated compositional isopleths for garnet ( $X_{\text{Py}} = 0.21$ ) and plagioclase ( $X_{\text{An}} = 0.41$ ) solid solutions. This assemblage was subsequently overprinted by the assemblage Hbl-Grt-Opx-Cpx-Pl-Ilm-Qtz assemblage during the retrograde stage ( $M_{1R}$ ) implying a drop in pressure down to ~7 kbar, 700–750 °C. This supports the results of thermobarometric analysis showing that the evolution was dominated by decompression accompanied by moderate cooling.

For the pelitic granulites, we chose the system  $\text{Na}_2\text{O}$ - $\text{CaO}$ - $\text{K}_2\text{O}$ - $\text{FeO}$ - $\text{MgO}$ - $\text{MnO}$ - $\text{Al}_2\text{O}_3$ - $\text{SiO}_2$ - $\text{TiO}_2$ - $\text{H}_2\text{O}$  (NCKFMASHTMn) that encompasses almost all the important mineral phases. Activity models for solid solution phases are taken from Holland and Powell (1998). The resultant phase diagram (Fig. 8c) contains several high-variance and low-variance fields separated by important reactions. Appearance and disappearance of key mineral phases are also shown in this diagram. Thus the 'Melt-in' curve shows steep slope (almost pressure insensitive) around 820 °C. Disappearance of cordierite is pressure sensitive and the diagram shows that cordierite cannot stabilize over 7.5 kbar pressures. In the central part of the diagram, a very small field of  $\text{Grt}$ - $\text{Crd}$ - $\text{Opx}$ - $\text{Rt}$ - $\text{Qtz}$ - $\text{Pl}$ - $\text{Kfs}$ - $\text{L}$  actually represents the peak metamorphic ( $M_2$ ) assemblage found in the studied rock (RNG 62b). This field has a pressure-temperature window of 6.0 kbar, 840–850 °C within which the peak metamorphic stage was achieved. We plotted calculated compositional isopleths for garnet and plagioclase in the pseudosection. The observed  $X_{\text{Py}}^{\text{Grt}}$  and  $X_{\text{An}}^{\text{Pl}}$  values pass through this  $P$ - $T$  range (Fig. 8d). The peak  $P$ - $T$  stage was achieved through dehydration melting of biotite-sillimanite-quartz-rutile-bearing assemblage as shown along the prograde arrow in Fig. 8d. The peak assemblage was changed to biotite-quartz-ilmenite-garnet-bearing assemblage as shown along the retrograde arrow. The overall sense of the  $M_2$  granulite-grade reworking is thus a heating-cooling type. This is also supported by textural, thermobarometric and geochronological data (U-Pb zircon SHRIMP dating by Bose et al., 2013).

## 5. Discussion

Petrological and microstructural studies show that the early high-pressure metamorphism ( $M_1$ ) in the mafic granulite produced the granoblastic fabric which locally assumes mylonitic character. The grain-scale early ( $M_1$ ) fabric in mafic granulite is correlatable with outcrop-scale  $D_{1M}$  fabric observed in the host charnockite suite. The dominant deformation in the charnockite mylonite is correlated with thrusting ( $D_{2M}$  event) of the granulite suite against SC along the Sukinda Thrust.  $D_{2M}$  shear-related fabric in mafic granulite enclaves and charnockite suite is essentially defined by grain refinement of newly produced hornblende within shear

showing intergrown quartz (Qtz). (c) BSE image showing vermicular intergrowth of garnet and quartz (Grt + Qtz) as overgrowth on porphyroblastic garnet (Grt) grain in pelitic granulite sample RNG 61B. Note the presence of monazite (Mnz) grain within the intergrowth. (d) Randomly oriented sillimanite (Sil) and biotite (Bt) grains within garnet (Grt) porphyroblasts in pelitic granulite sample RNG 61B. (e) Photomicrograph showing thin film of alkali feldspar (Kfs) developing between quartz (Qtz) and plagioclase (Pl) grains in the leucosome layer of sample RNG 61B. Also note the presence of biotite (Bt) selvage surrounding the leucosome. (f) Photomicrograph showing coarse garnet (Grt) and cordierite (Crd) forming granoblastic assemblage. A foliation is present in the matrix which is composed of biotite + sillimanite (Bt + Sil). (g) BSE image of orthopyroxene megacryst in ultramafic granulite sample JK 35 showing exsolved plagioclase (Pl) along prominent crystallographic orientation. The plagioclase collar separates the megacryst from the matrix. (h) Megacrystic orthopyroxene (Opx) surrounded by finer recrystallized aggregate of clinopyroxene + orthopyroxene  $\pm$  hornblende (Cpx + Opx  $\pm$  Hbl) in the same ultramafic granulite. Note the presence of plagioclase (Pl) surrounding the megacryst.

**Table 1**  
Representative phase chemical data from mafic granulites.

| Sample                         | JK 4B  |        |       |          |          |        |       |        |        |        |        |        |        |       |
|--------------------------------|--------|--------|-------|----------|----------|--------|-------|--------|--------|--------|--------|--------|--------|-------|
| Phase                          | Grt    |        | Cpx   |          |          | Pl     |       |        | Hbl    |        |        | Bt     | Ilm    | Opx   |
| Anal. No.                      | 17     | 19     | 14    | 15       | 16       | 24     | 33    | 38     | 1      | 2      | 9      | 10     | 12     | 11    |
| Type                           | Rim    | Core   | Core  | Core     | Rim      | Core   | Rim   | Rim    | Incl   | Incl   | Mat    | Rep    | Mat    | Mat   |
| SiO <sub>2</sub>               | 38.05  | 37.57  | 51.20 | 51.63    | 51.84    | 63.67  | 64.02 | 65.15  | 41.65  | 41.73  | 41.25  | 36.51  | 0.05   | 52.19 |
| TiO <sub>2</sub>               | 0.00   | 0.00   | 0.15  | 0.13     | 0.09     | 0.08   | 0.01  | 0.00   | 2.52   | 2.55   | 1.96   | 5.26   | 48.78  | 0.08  |
| Al <sub>2</sub> O <sub>3</sub> | 20.54  | 20.37  | 2.41  | 2.45     | 1.64     | 22.71  | 21.96 | 22.16  | 11.03  | 11.03  | 11.43  | 12.95  | 0.05   | 0.54  |
| Cr <sub>2</sub> O <sub>3</sub> | 0.12   | 0.00   | 0.08  | 0.00     | 0.00     | 0.00   | 0.00  | 0.19   | 0.01   | 0.01   | 0.00   | 0.01   | 0.14   | 0.00  |
| Fe <sub>2</sub> O <sub>3</sub> | 1.56   | 3.45   | 0.0   | 0.0      | 0.0      | 0.03   | 0.64  | 0.60   |        |        |        |        | 8.24   | 0     |
| FeO                            | 28.72  | 27.68  | 13.96 | 11.72    | 12.10    |        |       |        | 17.37  | 17.01  | 18.87  | 19.82  | 42.34  | 29.06 |
| MnO                            | 1.38   | 1.42   | 0.03  | 0.13     | 0.18     | 0.06   | 0.19  | 0.00   | 0.00   | 0.02   | 0.12   | 0.14   | 0.29   | 0.36  |
| MgO                            | 4.22   | 4.07   | 11.28 | 11.38    | 12.03    | 0.00   | 0.19  | 0.21   | 10.09  | 10.20  | 9.82   | 11.66  | 0.72   | 16.80 |
| CaO                            | 6.13   | 6.55   | 18.96 | 20.96    | 20.96    | 4.12   | 3.89  | 3.56   | 10.67  | 11.00  | 10.98  | 0.00   | 0.00   | 0.47  |
| ZnO                            | 0.00   | 0.20   | 0.00  | 0.00     | 0.23     | 0.00   | 0.10  | 0.00   | 0.26   | 0.19   | 0.17   | 0.39   | 0.00   | 0.00  |
| BaO                            | 0.00   | 0.01   | 0.04  | 0.00     | 0.01     | 0.00   | 0.02  | 0.00   | 0.00   | 0.00   | 0.00   | 0.74   | 0.00   | 0.00  |
| Na <sub>2</sub> O              | 0.04   | 0.00   | 1.35  | 1.39     | 1.09     | 9.03   | 7.97  | 7.99   | 2.09   | 2.11   | 2.06   | 0.07   | 0.01   | 0.00  |
| K <sub>2</sub> O               | 0.00   | 0.02   | 0.00  | 0.01     | 0.00     | 0.39   | 0.53  | 0.36   | 1.74   | 1.78   | 1.87   | 9.51   | 0.00   | 0.00  |
| P <sub>2</sub> O <sub>5</sub>  | 0.00   | 0.02   | 0.02  | 0.03     | 0.05     | 0.04   | 0.01  | 0.01   |        | 0.00   | 0.01   |        | 0.01   | 0.00  |
| F                              |        |        |       |          |          |        |       |        |        |        |        | 0.34   |        |       |
| H <sub>2</sub> O               |        |        |       |          |          |        |       |        |        |        |        | 3.78   |        |       |
| O = F, Cl                      |        |        |       |          |          |        |       |        |        |        |        | 0.14   |        |       |
| Total                          | 100.76 | 101.35 | 99.47 | 99.82    | 100.21   | 100.11 | 99.52 | 100.22 | 97.42  | 97.61  | 98.53  | 101.05 | 100.62 | 99.50 |
| O-basis                        | 12     | 6      | 8     | 22+2(OH) | 20+4(OH) | 2      | 6     |        |        |        |        |        |        |       |
| Si                             | 3.25   | 3.20   | 1.972 | 1.972    | 1.974    | 3.062  | 3.111 | 3.140  | 6.287  | 6.300  | 6.184  | 5.554  | 0.001  | 2.012 |
| Ti                             | 0.00   | 0.00   | 0.004 | 0.004    | 0.003    | 0.003  | 0.000 | 0.000  | 0.286  | 0.290  | 0.221  | 0.602  | 0.919  | 0.002 |
| Al                             | 1.39   | 1.37   | 0.109 | 0.110    | 0.074    | 1.287  | 1.257 | 1.259  | 1.962  | 1.963  | 2.019  | 2.322  | 0.001  | 0.025 |
| Cr                             | 0.01   | 0.00   | 0.002 | 0.000    | 0.000    | 0.000  | 0.000 | 0.007  | 0.001  | 0.001  | 0.000  | 0.001  | 0.003  | 0.000 |
| Fe <sup>3+</sup>               | 0.10   | 0.22   | 0.000 | 0.000    | 0.000    | 0.001  | 0.012 | 0.011  | 0.434  | 0.294  | 0.649  |        | 0.155  | 0.000 |
| Fe <sup>2+</sup>               | 2.05   | 1.97   | 0.449 | 0.374    | 0.385    |        |       |        | 1.759  | 1.853  | 1.716  | 2.521  | 0.887  | 0.937 |
| Mn                             | 0.10   | 0.10   | 0.001 | 0.004    | 0.006    | 0.00   | 0.01  | 0.000  | 0.000  | 0.003  | 0.015  | 0.018  | 0.006  | 0.012 |
| Mg                             | 0.54   | 0.52   | 0.647 | 0.648    | 0.683    | 0.00   | 0.01  | 0.015  | 2.271  | 2.296  | 2.195  | 2.644  | 0.027  | 0.966 |
| Ca                             | 0.56   | 0.60   | 0.782 | 0.858    | 0.855    | 0.21   | 0.20  | 0.184  | 1.726  | 1.779  | 1.764  | 0.000  | 0.000  | 0.019 |
| Zn                             | 0.00   | 0.01   | 0.000 | 0.000    | 0.007    | 0.00   | 0.00  | 0.000  | 0.029  | 0.021  | 0.019  | 0.044  | 0.000  | 0.000 |
| Ba                             | 0.00   | 0.00   | 0.001 | 0.000    | 0.000    | 0.00   | 0.00  | 0.000  | 0.000  | 0.000  | 0.000  | 0.044  | 0.000  | 0.000 |
| Na                             | 0.00   | 0.00   | 0.050 | 0.051    | 0.040    | 0.42   | 0.38  | 0.374  | 0.306  | 0.618  | 0.599  | 0.021  | 0.000  | 0.000 |
| K                              | 0.00   | 0.00   | 0.000 | 0.000    | 0.000    | 0.01   | 0.02  | 0.011  | 0.168  | 0.343  | 0.358  | 1.845  | 0.000  | 0.000 |
| P                              | 0.00   | 0.00   | 0.000 | 0.001    | 0.001    | 0.00   | 0.00  | 0.000  |        |        |        |        | 0.000  | 0.000 |
| F                              |        |        |       |          |          |        |       |        |        |        |        | 0.164  |        |       |
| OH                             |        |        |       |          |          |        |       |        |        |        |        | 3.836  |        |       |
| Total                          | 8.00   | 8.00   | 3.97  | 3.97     | 3.99     | 5.00   | 5.00  | 5.000  | 15.229 | 15.761 | 15.739 | 19.616 | 2.00   | 3.97  |
| X <sub>Mg</sub>                | 0.21   | 0.21   | 0.59  | 0.63     | 0.64     |        |       |        | 0.56   | 0.55   | 0.56   | 0.51   |        | 0.51  |
| X <sub>Py</sub>                | 0.17   | 0.16   |       |          |          |        |       |        |        |        |        |        |        |       |
| X <sub>Alm</sub>               | 0.63   | 0.62   |       |          |          |        |       |        |        |        |        |        |        |       |
| X <sub>Grs</sub>               | 0.17   | 0.19   |       |          |          |        |       |        |        |        |        |        |        |       |
| X <sub>Sps</sub>               | 0.03   | 0.03   |       |          |          |        |       |        |        |        |        |        |        |       |
| X <sub>Ab</sub>                |        |        |       |          |          | 0.65   | 0.63  | 0.66   |        |        |        |        |        |       |
| X <sub>An</sub>                |        |        |       |          |          | 0.33   | 0.34  | 0.32   |        |        |        |        |        |       |
| X <sub>Or</sub>                |        |        |       |          |          | 0.02   | 0.03  | 0.02   |        |        |        |        |        |       |
| X <sub>F</sub>                 |        |        |       |          |          |        |       |        |        |        |        | 0.04   |        |       |

| Sample                         | RNG 65A |        |        |       |            |        |        |       |        |       |       |       |        |       |       |    |
|--------------------------------|---------|--------|--------|-------|------------|--------|--------|-------|--------|-------|-------|-------|--------|-------|-------|----|
| Phase                          | Grt     |        | Cpx    |       |            | Grt    |        |       | Cpx    |       |       | Hbl   |        |       | Ilm   | Pl |
| Anal. No.                      | 11      | 48     | 49     | 50    | 51         | 58     | 59     | 60    | 62     | 71    | 65    | 66    | 68     | 46    | 8     |    |
| Type                           | Core    | Core   | Rim    | Rim   | Core       | Int    | Int    | Int   | Int    | Inc   | Mat   | Mat   | Inc    | Mat   | Core  |    |
| SiO <sub>2</sub>               | 38.72   | 38.41  | 38.14  | 50.81 | 51.45      | 38.17  | 38.56  | 38.44 | 52.88  | 42.26 | 42.35 | 40.74 | 0.03   | 58.89 | 60.75 |    |
| TiO <sub>2</sub>               | 0.03    | 0.00   | 0.06   | 0.36  | 0.25       | 0.12   | 0.27   | 0.00  | 0.11   | 2.06  | 1.72  | 1.89  | 47.46  | 0.00  | 0.01  |    |
| Al <sub>2</sub> O <sub>3</sub> | 21.71   | 21.19  | 20.92  | 3.26  | 3.08       | 21.11  | 20.99  | 20.86 | 2.14   | 11.97 | 13.19 | 13.79 | 0.01   | 25.18 | 23.85 |    |
| Cr <sub>2</sub> O <sub>3</sub> | 0.01    | 0.00   | 0.00   | 0.00  | 0.00       | 0.10   | 0.05   | 0.00  | 0.12   | 0.04  | 0.14  | 0.01  | 0.00   | 0.13  | 0.03  |    |
| Fe <sub>2</sub> O <sub>3</sub> | 0       | 1.63   | 3.05   | 0.00  | 0.00       | 0.00   | 1.74   | 0.10  | 0.00   |       |       |       | 12.09  | 0.11  | 0.39  |    |
| FeO                            | 26.15   | 24.59  | 24.48  | 8.62  | 9.59       | 25.20  | 24.36  | 24.88 | 8.35   | 14.02 | 14.52 | 15.34 | 40.19  |       |       |    |
| MnO                            | 0.79    | 0.65   | 0.84   | 0.02  | 0.22       | 0.57   | 0.79   | 0.59  | 0.00   | 0.00  | 0.05  | 0.00  | 0.33   | 0.02  | 0.01  |    |
| MgO                            | 5.46    | 5.24   | 4.81   | 11.99 | 12.49      | 5.03   | 4.79   | 4.84  | 14.06  | 10.90 | 11.45 | 10.02 | 1.13   | 0.01  | 0.02  |    |
| CaO                            | 7.52    | 8.86   | 9.16   | 22.03 | 22.38      | 9.97   | 9.87   | 9.25  | 23.04  | 11.63 | 11.51 | 11.50 | 0.00   | 7.99  | 5.27  |    |
| ZnO                            | 0       | 0.00   | 0.00   | 0.00  | 0.00       | 0.00   | 0.00   | 0.00  | 0.03   | 0.00  | 0.00  | 0.00  | 0.21   | 0.14  | 0.00  |    |
| BaO                            | 0       | 0.00   | 0.00   | 0.00  | 0.00       | 0.00   | 0.00   | 0.00  | 0.00   | 0.00  | 0.00  | 0.00  | 0.00   | 0.00  | 0.00  |    |
| Na <sub>2</sub> O              | 0.01    | 0.04   | 0.00   | 0.95  | 0.97       | 0.00   | 0.02   | 0.02  | 0.74   | 2.02  | 1.84  | 2.01  | 0.00   | 6.85  | 8.31  |    |
| K <sub>2</sub> O               | 0       | 0.00   | 0.00   | 0.00  | 0.00       | 0.03   | 0.00   | 0.06  | 0.00   | 1.05  | 1.07  | 1.25  | 0.03   | 0.23  | 0.22  |    |
| P <sub>2</sub> O <sub>5</sub>  | 0       | 0.00   | 0.00   | 0.01  | 0.00       | 0.00   | 0.06   | 0.00  | 0.06   | 0.00  | 0.00  | 0.04  | 0.00   | 0.02  | 0.00  |    |
| Total                          | 100.40  | 100.59 | 101.47 | 98.05 | 100.44     | 100.30 | 101.49 | 99.05 | 101.54 | 95.94 | 97.83 | 96.60 | 101.48 | 99.57 | 98.84 |    |
| O-basis                        | 12      | 6      | 12     | 6     | 20+2(F+OH) | 3      | 8      |       |        |       |       |       |        |       |       |    |
| Si                             | 3.005   | 2.983  | 2.953  | 1.946 | 1.935      | 2.980  | 2.978  | 3.028 | 1.952  | 6.394 | 6.217 | 6.145 | 0.001  | 2.826 | 2.952 |    |
| Ti                             | 0.002   | 0.000  | 0.003  | 0.010 | 0.007      | 0.007  | 0.016  | 0.000 | 0.003  | 0.234 | 0.190 | 0.214 | 0.886  | 0.000 | 0.000 |    |

Table 1 (continued)

| Sample           | RNG 65A |       |       |       |       |       |       |       |       |        |        |        |       |       |       |
|------------------|---------|-------|-------|-------|-------|-------|-------|-------|-------|--------|--------|--------|-------|-------|-------|
| Phase            | Grt     |       |       | Cpx   |       | Grt   |       |       | Cpx   | Hbl    |        |        | Ilm   | Pl    |       |
| Anal. No.        | 11      | 48    | 49    | 50    | 51    | 58    | 59    | 60    | 62    | 71     | 65     | 66     | 68    | 46    | 8     |
| Type             | Core    | Core  | Rim   | Rim   | Core  | Int   | Int   | Int   | Int   | Inc    | Mat    | Mat    | Inc   | Mat   | Core  |
| Al               | 1.986   | 1.939 | 1.909 | 0.147 | 0.137 | 1.943 | 1.910 | 1.937 | 0.093 | 2.134  | 2.282  | 2.451  | 0.000 | 1.424 | 1.366 |
| Cr               | 0.001   | 0.000 | 0.000 | 0.000 | 0.000 | 0.006 | 0.003 | 0.000 | 0.004 | 0.005  | 0.015  | 0.001  | 0.000 | 0.005 | 0.001 |
| Fe <sup>3+</sup> | 0       | 0.095 | 0.178 | 0.000 | 0.000 | 0.000 | 0.101 | 0.006 | 0.000 | 0.038  | 0.542  | 0.283  | 0.226 | 0.002 | 0.007 |
| Fe <sup>2+</sup> | 1.697   | 1.597 | 1.586 | 0.276 | 0.302 | 1.645 | 1.573 | 1.640 | 0.258 | 1.736  | 1.240  | 1.652  | 0.834 |       |       |
| Mn               | 0.052   | 0.043 | 0.055 | 0.001 | 0.007 | 0.038 | 0.052 | 0.040 | 0.000 | 0      | 0.006  | 0      | 0.007 | 0.001 | 0.000 |
| Mg               | 0.631   | 0.606 | 0.556 | 0.685 | 0.700 | 0.586 | 0.551 | 0.569 | 0.774 | 2.459  | 2.506  | 2.253  | 0.042 | 0.000 | 0.001 |
| Ca               | 0.625   | 0.737 | 0.760 | 0.904 | 0.902 | 0.834 | 0.817 | 0.780 | 0.912 | 1.885  | 1.811  | 1.859  | 0.000 | 0.411 | 0.274 |
| Zn               | 0       | 0.000 | 0.000 | 0.000 | 0.000 | 0.000 | 0.000 | 0.000 | 0.001 | 0      | 0.000  | 0      | 0.004 | 0.005 | 0.000 |
| Ba               | 0       | 0.000 | 0.000 | 0.000 | 0.000 | 0.000 | 0.000 | 0.000 | 0.000 | 0      | 0.000  | 0      | 0.000 | 0.000 | 0.000 |
| Na               | 0.001   | 0.003 | 0.000 | 0.035 | 0.035 | 0.000 | 0.001 | 0.001 | 0.026 | 0.593  | 0.524  | 0.588  | 0.000 | 0.319 | 0.391 |
| K                | 0       | 0.000 | 0.000 | 0.000 | 0.000 | 0.001 | 0.000 | 0.003 | 0.000 | 0.203  | 0.200  | 0.241  | 0.001 | 0.007 | 0.007 |
| P                | 0       | 0.000 | 0.000 | 0.000 | 0.000 | 0.000 | 0.002 | 0.000 | 0.001 |        |        |        | 0.000 | 0.000 | 0.000 |
| Total            | 8.000   | 8.000 | 8.000 | 3.97  | 3.99  | 8.038 | 8.000 | 8.000 | 4.00  | 15.681 | 15.533 | 15.687 | 2.00  | 5.00  | 5.000 |
| X <sub>Mg</sub>  | 0.27    | 0.28  | 0.26  | 0.71  | 0.70  | 0.26  | 0.26  | 0.26  | 0.75  | 0.59   | 0.67   | 0.58   |       |       |       |
| X <sub>Py</sub>  | 0.21    | 0.20  | 0.19  |       |       | 0.19  | 0.18  | 0.19  |       |        |        |        |       |       |       |
| X <sub>Alm</sub> | 0.56    | 0.54  | 0.54  |       |       | 0.53  | 0.53  | 0.54  |       |        |        |        |       |       |       |
| X <sub>Grs</sub> | 0.21    | 0.25  | 0.26  |       |       | 0.27  | 0.27  | 0.26  |       |        |        |        |       |       |       |
| X <sub>Sps</sub> | 0.02    | 0.01  | 0.02  |       |       | 0.01  | 0.02  | 0.01  |       |        |        |        |       |       |       |
| X <sub>Ab</sub>  |         |       |       |       |       |       |       |       |       |        |        |        |       | 0.43  | 0.58  |
| X <sub>An</sub>  |         |       |       |       |       |       |       |       |       |        |        |        |       | 0.56  | 0.41  |
| X <sub>Or</sub>  |         |       |       |       |       |       |       |       |       |        |        |        |       | 0.01  | 0.01  |

Core—core of pophryroblast; Rim—rim of porphyroblast; Inc—inclusion; Mat—matrix; Rep—replacement; Int—intergrowth.

X<sub>Mg</sub> = Mg/(Mg + Fe<sup>2+</sup>); X<sub>Py</sub> = Mg/(Mg + Fe<sup>2+</sup> + Ca + Mn); X<sub>Alm</sub> = Fe<sup>2+</sup>/(Mg + Fe<sup>2+</sup> + Ca + Mn); X<sub>Grs</sub> = Ca/(Mg + Fe<sup>2+</sup> + Ca + Mn).

X<sub>Sps</sub> = Mn/(Mg + Fe<sup>2+</sup> + Ca + Mn); X<sub>An</sub> = Ca/(Ca + Na + K); X<sub>Ab</sub> = Na/(Ca + Na + K); X<sub>Or</sub> = K/(Ca + Na + K).

Table 2

Representative phase chemical data from pelitic granulites.

| Sample                         | RNG 62b |        |       |        |       |       |        |       |        |       |       |       |       |  |
|--------------------------------|---------|--------|-------|--------|-------|-------|--------|-------|--------|-------|-------|-------|-------|--|
| Phase                          | Grt     |        |       | Opx    |       |       |        | Pl    | Grt    | Crd   |       | Bt    |       |  |
| Anal. No.                      | 1       | 8      | 14    | 40     | 41    | 42    | 43     | 80    | 79     | 88    | 89    | 91    | 85    |  |
| Type                           | Rim     | Rim    | Core  | Core   | Rim   | Rim   | Rim    | Mat   | Int    | Mat   | Mat   | Inc   | Mat   |  |
| SiO <sub>2</sub>               | 39.13   | 39.28  | 39.53 | 52.04  | 51.09 | 50.90 | 50.95  | 59.05 | 38.68  | 49.51 | 50.01 | 39.06 | 37.60 |  |
| TiO <sub>2</sub>               | 0.03    | 0.00   | 0.00  | 0.06   | 0.90  | 0.04  | 0.06   | 0.02  | 0.00   | 0.02  | 0.00  | 0.35  | 5.11  |  |
| Al <sub>2</sub> O <sub>3</sub> | 21.94   | 22.24  | 21.74 | 4.17   | 3.92  | 5.41  | 4.78   | 25.64 | 22.03  | 33.30 | 33.47 | 20.79 | 15.09 |  |
| Cr <sub>2</sub> O <sub>3</sub> | 0.00    | 0.14   | 0.01  | 0.29   | 0.15  | 0.14  | 0.24   | 0.00  | 0.21   | 0.00  | 0.00  | 0.13  | 0.60  |  |
| Fe <sub>2</sub> O <sub>3</sub> | 2.12    | 2.29   | 0.00  | 1.55   | 0.00  | 0.00  | 2.50   | 0.10  | 1.21   | 1.52  | 1.13  |       |       |  |
| FeO                            | 25.94   | 25.37  | 26.00 | 19.58  | 19.32 | 19.04 | 18.20  |       | 25.66  | 1.59  | 1.95  | 6.55  | 9.62  |  |
| MnO                            | 0.32    | 0.55   | 0.34  | 0.16   | 0.11  | 0.24  | 0.20   | 0.07  | 0.51   | 0.01  | 0.05  | 0.09  | 0.00  |  |
| MgO                            | 10.60   | 10.83  | 10.35 | 23.83  | 23.19 | 23.16 | 23.85  | 0.00  | 10.24  | 12.19 | 12.25 | 19.31 | 16.79 |  |
| CaO                            | 1.30    | 1.36   | 1.78  | 0.05   | 0.13  | 0.04  | 0.05   | 7.54  | 1.32   | 0.01  | 0.01  | 0.17  | 0.00  |  |
| ZnO                            | 0.00    | 0.00   | 0.08  | 0.00   | 0.00  | 0.00  | 0.00   | 0.11  | 0.15   | 0.18  | 0.00  | 0.00  | 0.00  |  |
| BaO                            | 0.00    | 0.00   | 0.01  | 0.00   | 0.00  | 0.00  | 0.00   | 0.00  | 0.00   | 0.02  | 0.00  | 0.02  | 0.45  |  |
| Na <sub>2</sub> O              | 0.00    | 0.04   | 0.02  | 0.00   | 0.02  | 0.01  | 0.04   | 7.07  | 0.04   | 0.04  | 0.03  | 0.08  | 0.00  |  |
| K <sub>2</sub> O               | 0.00    | 0.00   | 0.03  | 0.00   | 0.03  | 0.03  | 0.00   | 0.16  | 0.00   | 0.00  | 0.02  | 7.32  | 9.88  |  |
| P <sub>2</sub> O <sub>5</sub>  | 0.06    | 0.05   | 0.07  | 0.00   | 0.00  | 0.01  | 0.02   | 0.05  | 0.03   | 0.00  | 0.00  |       |       |  |
| F                              |         |        |       |        |       |       |        | 0.05  | 0.00   | 0.10  | 0.04  | 0.59  | 0.25  |  |
| H <sub>2</sub> O               |         |        |       |        |       |       |        |       |        |       |       | 3.94  | 3.97  |  |
| O = F, Cl                      |         |        |       |        |       |       |        |       |        |       |       | 0.25  | 0.11  |  |
| Total                          | 101.43  | 102.14 | 99.95 | 101.72 | 98.86 | 99.00 | 100.89 | 99.86 | 100.08 | 98.49 | 98.96 | 98.14 | 99.26 |  |
| Si                             | 2.960   | 2.95   | 3.023 | 1.884  | 1.90  | 1.88  | 1.858  | 2.82  | 2.964  | 4.97  | 4.99  | 5.550 | 5.521 |  |
| Ti                             | 0.002   | 0.00   | 0.000 | 0.001  | 0.03  | 0.00  | 0.002  | 0.00  | 0.000  | 0.00  | 0.00  | 0.037 | 0.564 |  |
| Al                             | 1.956   | 1.97   | 1.959 | 0.178  | 0.17  | 0.24  | 0.205  | 1.45  | 1.989  | 3.94  | 3.94  | 3.482 | 2.612 |  |
| Cr                             | 0.000   | 0.01   | 0.001 | 0.008  | 0.00  | 0.00  | 0.007  | 0.00  | 0.013  | 0.00  | 0.00  | 0.015 | 0.070 |  |
| Fe <sup>3+</sup>               | 0.121   | 0.13   | 0.000 | 0.042  | 0.00  | 0.00  | 0.069  | 0.00  | 0.070  | 0.11  | 0.09  |       |       |  |
| Fe <sup>2+</sup>               | 1.641   | 1.59   | 1.663 | 0.593  | 0.60  | 0.59  | 0.555  |       | 1.645  | 0.13  | 0.16  | 0.778 | 1.181 |  |
| Mn                             | 0.020   | 0.03   | 0.022 | 0.005  | 0.00  | 0.01  | 0.006  | 0.00  | 0.033  | 0.00  | 0.00  | 0.011 | 0.000 |  |
| Mg                             | 1.195   | 1.21   | 1.179 | 1.286  | 1.28  | 1.28  | 1.296  | 0.00  | 1.170  | 1.82  | 1.82  | 4.090 | 3.675 |  |
| Ca                             | 0.105   | 0.11   | 0.146 | 0.002  | 0.01  | 0.00  | 0.002  | 0.39  | 0.108  | 0.00  | 0.00  | 0.026 | 0.000 |  |
| Zn                             | 0.000   | 0.00   | 0.005 | 0.000  | 0.00  | 0.00  | 0.000  | 0.00  | 0.009  | 0.01  | 0.00  | 0.000 | 0.000 |  |
| Ba                             | 0.000   | 0.00   | 0.000 | 0.000  | 0.00  | 0.00  | 0.000  | 0.00  | 0.000  | 0.00  | 0.00  | 0.001 | 0.026 |  |
| Na                             | 0.000   | 0.00   | 0.001 | 0.000  | 0.00  | 0.00  | 0.001  | 0.33  | 0.003  | 0.00  | 0.00  | 0.022 | 0.000 |  |
| K                              | 0.000   | 0.00   | 0.002 | 0.000  | 0.00  | 0.00  | 0.000  | 0.01  | 0.000  | 0.00  | 0.00  | 1.327 | 1.850 |  |
| P                              | 0.002   | 0.00   | 0.002 | 0.000  | 0.00  | 0.00  | 0.000  | 0.00  | 0.001  | 0.00  | 0.00  |       |       |  |
| OH                             |         |        |       |        |       |       |        |       |        |       |       | 3.735 | 3.884 |  |

(continued on next page)



Table 2 (continued)

| Sample           | RNG 62b |      |       |      |      |      |       |      |      |       |       |        |        |
|------------------|---------|------|-------|------|------|------|-------|------|------|-------|-------|--------|--------|
| Phase            | Grt     |      |       | Opx  |      |      |       | Pl   | Grt  | Crd   |       | Bt     |        |
| Anal. No.        | 1       | 8    | 14    | 40   | 41   | 42   | 43    | 80   | 79   | 88    | 89    | 91     | 85     |
| Type             | Rim     | Rim  | Core  | Core | Rim  | Rim  | Rim   | Mat  | Int  | Mat   | Mat   | Inc    | Mat    |
| F                |         |      |       |      |      |      |       |      |      |       |       | 0.265  | 0.116  |
| Sum              | 8.00    | 8.00 | 7.997 | 4.00 | 3.99 | 4.00 | 4.000 | 5.00 | 8.00 | 11.00 | 11.00 | 19.339 | 19.499 |
| X <sub>Mg</sub>  | 0.42    | 0.43 | 0.41  | 0.68 | 0.68 | 0.68 | 0.70  |      | 0.42 | 0.93  | 0.92  | 0.84   | 0.76   |
| X <sub>Py</sub>  | 0.40    | 0.41 | 0.39  |      |      |      |       |      | 0.40 |       |       |        |        |
| X <sub>Alm</sub> | 0.55    | 0.54 | 0.55  |      |      |      |       |      | 0.56 |       |       |        |        |
| X <sub>Grs</sub> | 0.01    | 0.01 | 0.01  |      |      |      |       |      | 0.01 |       |       |        |        |
| X <sub>Sps</sub> | 0.01    | 0.01 | 0.01  |      |      |      |       |      | 0.01 |       |       |        |        |
| X <sub>An</sub>  |         |      |       |      |      |      |       | 0.54 |      |       |       |        |        |
| X <sub>Ab</sub>  |         |      |       |      |      |      |       | 0.46 |      |       |       |        |        |
| X <sub>Or</sub>  |         |      |       |      |      |      |       | 0.01 |      |       |       |        |        |
| X <sub>F</sub>   |         |      |       |      |      |      |       |      |      |       |       | 0.07   | 0.03   |

| Sample                         | RNG 61B |        |        |       |        |        |       |        |        |  |
|--------------------------------|---------|--------|--------|-------|--------|--------|-------|--------|--------|--|
| Phase                          | Grt     |        |        | Crd   | Sil    | Kfs    |       | Pl     |        |  |
| Anal. No.                      | 50      | 58     | 60     | 57    | 56     | 53     | 54    | 51     | 52     |  |
| Type                           | Mat     | Mat    | Mat    | Mat   | Inc    | Host   | Host  | Lam    | Lam    |  |
| SiO <sub>2</sub>               | 38.77   | 39.46  | 39.13  | 49.66 | 37.04  | 64.16  | 63.98 | 64.33  | 63.90  |  |
| TiO <sub>2</sub>               | 0.03    | 0.02   | 0.00   | 0.00  | 0.01   | 0.00   | 0.00  | 0.00   | 0.00   |  |
| Al <sub>2</sub> O <sub>3</sub> | 21.97   | 22.07  | 22.08  | 33.03 | 62.33  | 18.76  | 18.33 | 22.70  | 23.03  |  |
| Cr <sub>2</sub> O <sub>3</sub> | 0.11    | 0.02   | 0.03   | 0.00  | 0.09   | 0.00   | 0.00  | 0.00   | 0.10   |  |
| Fe <sub>2</sub> O <sub>3</sub> | 3.13    | 0.41   | 1.86   | 2.30  |        |        |       |        |        |  |
| FeO                            | 26.77   | 27.76  | 26.96  | 1.80  | 1.07   | 0.06   | 0.00  | 0.08   | 0.00   |  |
| MnO                            | 0.42    | 0.29   | 0.20   | 0.00  | 0.07   | 0.00   | 0.00  | 0.00   | 0.00   |  |
| MgO                            | 10.17   | 10.19  | 10.44  | 12.14 | 0.00   | 0.02   | 0.01  | 0.00   | 0.01   |  |
| CaO                            | 0.82    | 0.63   | 0.71   | 0.00  | 0.03   | 0.00   | 0.03  | 3.94   | 4.62   |  |
| ZnO                            | 0.01    | 0.20   | 0.12   | 0.08  | 0.00   | 0.00   | 0.00  | 0.00   | 0.06   |  |
| BaO                            | 0.01    | 0.00   | 0.00   | 0.00  | 0.00   | 1.19   | 1.23  | 0.13   | 0.00   |  |
| Na <sub>2</sub> O              | 0.00    | 0.01   | 0.00   | 0.08  | 0.00   | 1.03   | 1.11  | 8.21   | 9.05   |  |
| K <sub>2</sub> O               | 0.00    | 0.00   | 0.02   | 0.00  | 0.00   | 14.74  | 14.85 | 2.40   | 0.44   |  |
| P <sub>2</sub> O <sub>5</sub>  | 0.02    | 0.04   | 0.00   | 0.03  | 0.00   | 0.05   | 0.05  | 0.07   | 0.11   |  |
| Total                          | 102.22  | 101.09 | 101.55 | 99.12 | 100.64 | 100.03 | 99.59 | 101.86 | 101.31 |  |
| Si                             | 2.93    | 3.00   | 2.96   | 4.967 | 0.997  | 3.30   | 3.31  | 3.07   | 3.04   |  |
| Ti                             | 0.00    | 0.00   | 0.00   | 0.000 | 0.000  | 0.00   | 0.00  | 0.00   | 0.00   |  |
| Al                             | 1.96    | 1.98   | 1.97   | 3.893 | 1.978  | 1.14   | 1.12  | 1.28   | 1.29   |  |
| Cr                             | 0.01    | 0.00   | 0.00   | 0.000 | 0.002  | 0.00   | 0.00  | 0.00   | 0.00   |  |
| Fe <sup>3+</sup>               | 0.18    | 0.02   | 0.11   | 0.173 | 0.022  | 0.00   | 0.00  | 0.00   | 0.00   |  |
| Fe <sup>2+</sup>               | 1.69    | 1.76   | 1.71   | 0.151 |        |        |       |        |        |  |
| Mn                             | 0.03    | 0.02   | 0.01   | 0.000 | 0.002  | 0.00   | 0.00  | 0.00   | 0.00   |  |
| Mg                             | 1.15    | 1.15   | 1.18   | 1.811 | 0.000  | 0.00   | 0.00  | 0.00   | 0.00   |  |
| Ca                             | 0.07    | 0.05   | 0.06   | 0.000 | 0.001  | 0.00   | 0.00  | 0.20   | 0.24   |  |
| Zn                             | 0.00    | 0.01   | 0.01   | 0.006 | 0.000  | 0.00   | 0.00  | 0.00   | 0.00   |  |
| Ba                             | 0.00    | 0.00   | 0.00   | 0.000 | 0.000  | 0.02   | 0.02  | 0.00   | 0.00   |  |
| Na                             | 0.00    | 0.00   | 0.00   | 0.008 | 0.000  | 0.05   | 0.06  | 0.38   | 0.42   |  |
| K                              | 0.00    | 0.00   | 0.00   | 0.000 | 0.000  | 0.48   | 0.49  | 0.07   | 0.01   |  |
| P                              | 0.00    | 0.00   | 0.00   | 0.001 | 0.000  | 0.00   | 0.00  | 0.00   | 0.00   |  |
| Sum                            | 8.00    | 8.00   | 8.00   | 11.00 | 3.00   | 5.00   | 5.00  | 5.00   | 5.00   |  |
| X <sub>Mg</sub>                | 0.40    | 0.40   | 0.41   | 0.92  |        |        |       |        |        |  |
| X <sub>Py</sub>                | 0.39    | 0.39   | 0.40   |       |        |        |       |        |        |  |
| X <sub>Alm</sub>               | 0.58    | 0.59   | 0.58   |       |        |        |       |        |        |  |
| X <sub>Grs</sub>               | 0.02    | 0.02   | 0.02   |       |        |        |       |        |        |  |
| X <sub>Sps</sub>               | 0.01    | 0.01   | 0.00   |       |        |        |       |        |        |  |
| X <sub>An</sub>                |         |        |        |       |        | 0.00   | 0.00  | 0.31   | 0.35   |  |
| X <sub>Ab</sub>                |         |        |        |       |        | 0.10   | 0.10  | 0.58   | 0.63   |  |
| X <sub>Or</sub>                |         |        |        |       |        | 0.90   | 0.90  | 0.11   | 0.02   |  |

Core–core of porphyroblast; Rim – rim of porphyroblast; Inc – inclusion; Mat – matrix; Host – perthite host; Lam – exsolved lamellae.

X<sub>Mg</sub> = Mg/(Mg + Fe<sup>2+</sup>); X<sub>Py</sub> = Mg/(Mg + Fe<sup>2+</sup> + Ca + Mn); X<sub>Alm</sub> = Fe<sup>2+</sup>/(Mg + Fe<sup>2+</sup> + Ca + Mn); X<sub>Grs</sub> = Ca/(Mg + Fe<sup>2+</sup> + Ca + Mn).

X<sub>Sps</sub> = Mn/(Mg + Fe<sup>2+</sup> + Ca + Mn); X<sub>An</sub> = Ca/(Ca + Na + K); X<sub>Ab</sub> = Na/(Ca + Na + K); X<sub>Or</sub> = K/(Ca + Na + K); X<sub>F</sub> = F/(F + OH).

bands. The coarse-grained hornblende occurring outside the shear bands show development of tiny vermicular intergrowths of garnet-quartz-clinopyroxene along grain margins. Therefore, the most dominant D<sub>2M</sub> shearing event that controlled the dominant fabric development within the granulites can be temporally correlated with the M<sub>1R</sub> to M<sub>2</sub> events.

Textural, pseudosection and thermobarometric analyses indicate that M<sub>1</sub> metamorphism occurred at 10.0–12.0 kbar, 860 °C, stabilizing the assemblage Grt + Cpx + Pl + Qtz + Ilm ± Opx in mafic granulite and Opx + Cpx ± Pl in ultramafic granulite. A subsequent process of decompression subsequently brought the granulites to mid-crustal level (5.5–7.5 kbar). Therefore, the mafic

**Table 3**  
Representative phase chemical data from ultramafic granulite.

| Sample                         | JK 35 |        |       |       |       |        |       |       |       |       |
|--------------------------------|-------|--------|-------|-------|-------|--------|-------|-------|-------|-------|
|                                | Opx   | Opx    | Pl    | Pl    | Opx   | Opx    | Cpx   | Cpx   | Pl    | Pl    |
| Analysis No.                   | 2     | 1      | 3     | 4     | 11    | 13     | 9     | 19    | 12    | 14    |
| Type                           | Core  | CLX    | Ex    | Ex    | Mat   | Mat    | Mat   | Mat   | Crn   | Crn   |
| SiO <sub>2</sub>               | 50.67 | 52.26  | 59.55 | 59.24 | 52.86 | 53.16  | 53.00 | 52.46 | 59.52 | 59.69 |
| TiO <sub>2</sub>               | 0.79  | 0.00   | 0.00  | 0.00  | 0.25  | 0.00   | 0.00  | 0.32  | 0.00  | 0.00  |
| Al <sub>2</sub> O <sub>3</sub> | 3.05  | 1.26   | 24.97 | 24.79 | 0.75  | 1.05   | 1.53  | 1.79  | 24.90 | 25.27 |
| Cr <sub>2</sub> O <sub>3</sub> | 0.34  | 0.00   | 0.00  | 0.00  | 0.00  | 0.00   | 0.00  | 0.00  | 0.00  | 0.00  |
| Fe <sub>2</sub> O <sub>3</sub> | 0.39  | 1.39   | 0.75  | 1.12  | 0.00  | 0.09   | 0.00  | 0.00  | 0.00  | 0.00  |
| FeO                            | 20.88 | 21.72  |       |       | 23.38 | 22.37  | 8.47  | 9.24  |       |       |
| MnO                            | 0.00  | 0.62   | 0.00  | 0.00  | 0.00  | 0.34   | 0.00  | 0.32  | 0.00  | 0.00  |
| MgO                            | 20.36 | 21.68  | 0.00  | 0.00  | 22.00 | 22.70  | 13.10 | 13.28 | 0.00  | 0.00  |
| CaO                            | 3.22  | 1.17   | 6.65  | 7.00  | 0.63  | 0.31   | 23.44 | 22.05 | 7.27  | 7.10  |
| ZnO                            | 0.00  | 0.00   | 0.00  | 0.00  | 0.00  | 0.00   | 0.00  | 0.00  | 0.00  | 0.00  |
| BaO                            | 0.00  | 0.00   | 0.00  | 0.00  | 0.00  | 0.00   | 0.00  | 0.00  | 0.00  | 0.00  |
| Na <sub>2</sub> O              | 0.00  | 0.00   | 7.35  | 7.52  | 0.00  | 0.00   | 0.00  | 0.00  | 7.44  | 7.30  |
| K <sub>2</sub> O               | 0.20  | 0.00   | 0.31  | 0.00  | 0.00  | 0.00   | 0.00  | 0.00  | 0.17  | 0.17  |
| Total                          | 99.89 | 100.09 | 99.58 | 99.67 | 99.87 | 100.01 | 99.54 | 99.46 | 99.29 | 99.52 |
| Si                             | 1.900 | 1.953  | 2.871 | 2.857 | 1.977 | 1.976  | 1.982 | 1.968 | 2.862 | 2.862 |
| Ti                             | 0.022 | 0.000  | 0.000 | 0.000 | 0.007 | 0.000  | 0.000 | 0.009 | 0.000 | 0.000 |
| Al                             | 0.135 | 0.055  | 1.419 | 1.409 | 0.033 | 0.046  | 0.067 | 0.079 | 1.411 | 1.428 |
| Cr                             | 0.010 | 0.000  | 0.000 | 0.000 | 0.000 | 0.000  | 0.000 | 0.000 | 0.000 | 0.000 |
| Fe <sup>3+</sup>               | 0.011 | 0.039  | 0.014 | 0.020 | 0.000 | 0.002  | 0.000 | 0.000 | 0.000 | 0.000 |
| Fe <sup>2+</sup>               | 0.655 | 0.679  |       |       | 0.731 | 0.695  | 0.265 | 0.290 |       |       |
| Mn                             | 0.000 | 0.019  | 0.000 | 0.000 | 0.000 | 0.011  | 0.000 | 0.010 | 0.000 | 0.000 |
| Mg                             | 1.138 | 1.208  | 0.000 | 0.000 | 1.226 | 1.258  | 0.731 | 0.742 | 0.000 | 0.000 |
| Ca                             | 0.130 | 0.047  | 0.343 | 0.362 | 0.025 | 0.012  | 0.939 | 0.886 | 0.375 | 0.365 |
| Zn                             | 0.000 | 0.000  | 0.000 | 0.000 | 0.000 | 0.000  | 0.000 | 0.000 | 0.000 | 0.000 |
| Ba                             | 0.000 | 0.000  | 0.000 | 0.000 | 0.000 | 0.000  | 0.000 | 0.000 | 0.000 | 0.000 |
| Na                             | 0.000 | 0.000  | 0.344 | 0.351 | 0.000 | 0.000  | 0.000 | 0.000 | 0.347 | 0.339 |
| K                              | 0.005 | 0.000  | 0.010 | 0.000 | 0.000 | 0.000  | 0.000 | 0.000 | 0.005 | 0.005 |
| Sum                            | 4.00  | 4.00   | 5.00  | 5.00  | 4.00  | 4.00   | 3.98  | 3.98  | 5.00  | 5.00  |
| X <sub>Mg</sub>                | 0.63  | 0.64   |       |       | 0.63  | 0.64   | 0.73  | 0.72  |       |       |
| X <sub>Ab</sub>                |       |        | 0.49  | 0.49  |       |        |       |       | 0.48  | 0.48  |
| X <sub>An</sub>                |       |        | 0.49  | 0.51  |       |        |       |       | 0.52  | 0.51  |
| X <sub>Or</sub>                |       |        | 0.01  | 0.00  |       |        |       |       | 0.01  | 0.01  |

Core–core of megacryst; CLX–composition close to exsolved plagioclase; EX–Exsolved; Mat–matrix; Crn–Corona.

X<sub>Mg</sub> = Mg/(Mg + Fe<sup>2+</sup>); X<sub>An</sub> = Ca/(Ca + Na + K); X<sub>Ab</sub> = Na/(Ca + Na + K); X<sub>Or</sub> = K/(Ca + Na + K).

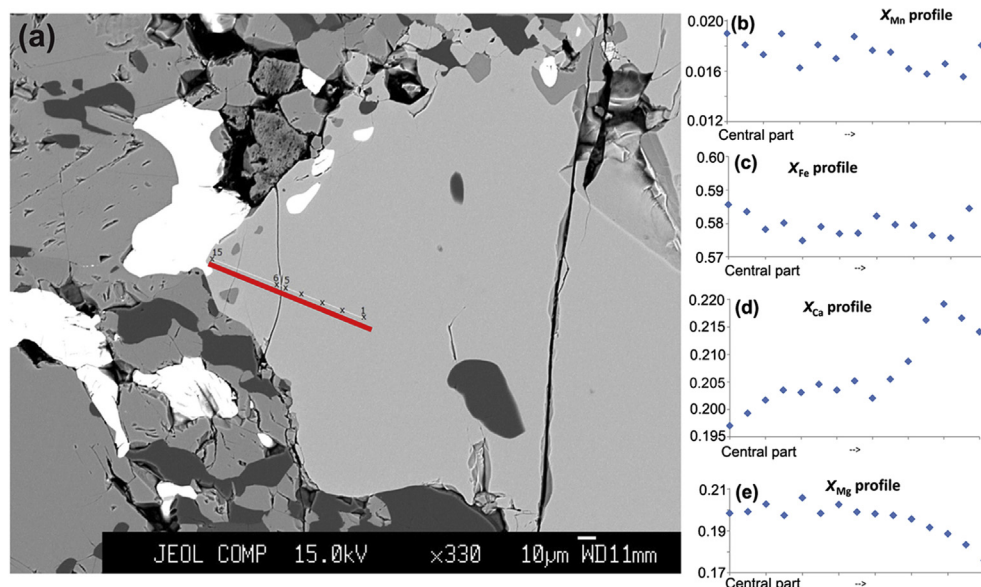


**Figure 7.** Partial compositional profile of garnet porphyroblast for selective elements in mafic granulite sample RNG 65A. (a) BSE image of the garnet grain where the line marking the profile path. (b)–(e) Profile for Mn, Fe<sup>2+</sup>, Ca and Mg respectively. Note the slight rimward decrease in Mg and increase in Ca.

**Table 4**  
Pressure-temperature estimates from studied granulite samples.

| Sample No. | Rock type            | Thermo/barometer used    | Model                            | Assumed P/T | Results (P/T)  |
|------------|----------------------|--------------------------|----------------------------------|-------------|--|
| JK4B       | Mafic granulite      | Grt-Cpx thermometer      | Ganguly (1979)                   | 10 Kbar     | 748–799 °C   |
| JK 14C     | Mafic granulite      |                          |                                  |             | 767–860 °C   |
| JK 19B     | Mafic granulite      |                          |                                  |             | 792–833 °C   |
| JK 8B      | Mafic granulite      |                          |                                  |             | 763–822 °C   |
| JK 14B     | Mafic granulite      |                          |                                  |             | 781–822 °C   |
| JK 14D     | Mafic granulite      |                          |                                  |             | 764–814 °C   |
| JK 20      | Mafic granulite      |                          |                                  |             | 784–786 °C   |
| RNG 65A    | Mafic granulite      | Cpx-Ilm thermometer      | Bishop (1980)                    |             | 789 °C   |
| RNG 65A    | Mafic granulite      | Grt-Ilm thermometer      | Pownceby et al. (1987)           |             | 595–719 °C   |
| JK4B       | Mafic granulite      |                          |                                  |             | 632–654 °C   |
| JK35       | Ultramafic granulite | Opx-Cpx thermometer      | Kretz (1982)                     |             | 772–831 °C   |
| JK 14C     | Mafic granulite      | Grt-Cpx-Pl-Qtz barometer | Moecher et al. (1988)            | 840 °C      | 11.8–12.1 Kbar   |
| JK 19B     | Mafic granulite      |                          |                                  |             | 11.2–12.2 Kbar   |
| JK 20      | Mafic granulite      |                          |                                  |             | 11.2 Kbar  |
| JK 4B      | Mafic granulite      |                          |                                  |             | 11.2–11.5 Kbar   |
| JK 14B     | Mafic granulite      |                          |                                  |             | 11.0–11.2 Kbar   |
| RNG 65A    | Mafic granulite      |                          |                                  |             | 11.0–11.5 Kbar   |
| JK35       | Ultramafic granulite | CaTs-Anorthite barometer | McCarthy and Patino Douce (1998) |             | 9.5–10.0 Kbar  |
| JK 4B      | Mafic granulite      | Hbl-Pl thermometer       | Holland and Blundy (1994)        | 6 Kbar      | 760–790 °C   |
| RNG 65A    | Mafic granulite      |                          |                                  |             | 770 °C   |
| RNG 65A    | Mafic granulite      | Grt-Hbd thermometer      | Ravna (2000)                     |             | 624–724 °C   |
| JK 4B      | Mafic granulite      | Hbd-Al barometer         | Anderson and Smith (1995)        | 700 °C      | 6.01 Kbar<br>5.98 kbar<br>6.24 Kbar<br>5.81 Kbar<br>5.47 Kbar<br>5.59 Kbar |
|            |                      |                          | Schmidt (1992)                   |             | 5.9–6.2 Kbar   |
| RNG 65A    | Mafic granulite      |                          | Anderson and Smith (1995)        |             | 5.5–7.5 Kbar   |
|            |                      |                          | Schmidt (1992)                   |             | 6.3 Kbar   |
| RNG 65A    | Mafic granulite      | Grt-Hbd barometer        | Kohn and Spear (1989)            | 700 °C      | 6.9–7.5 Kbar   |
| RNG 62b    | Pelitic granulite    | Grt-Opx thermometer      | Lee and Ganguly (1988)           | 6 Kbar      | 690–731 °C   |
|            |                      | Grt-Opx-Pl-Qtz barometer | Bhattacharya et al. (1991)       | 800 °C      | 5.7 Kbar   |
|            |                      | Grt-Opx-Pl-Qz (RCLC)     | Pattison et al. (2003)           |             | 679 °C, 5.8 Kbar   |
|            |                      | Grt-Crd thermometer      | Nichols et al. (1992)            | 6 Kbar      | 583–598 °C   |
|            |                      | Grt-Crd barometer        | Harris and Holland (1984)        |             | 4.1–4.3 Kbar   |
|            |                      | Grt-Bt thermometer       | Bhattacharya et al. (1992)       |             | 522–594 °C   |

granulite preserved an early metamorphic history in contrast to the pelitic granulites which only preserved the later imprint that is comparable with reworking of the mafic granulites in  $D_2$ – $M_2$ . Kar et al. (2003) also documented a high-pressure mineral assemblage (~12 kbar, 800 °C) from 'inclusions in charnockites' and suggested that it signifies a decompression melting of hornblende-bearing assemblage along a clockwise  $P$ - $T$  path. However, the implication of such high- $P$  metamorphic event was not explored further in their study. A recent study by Mahapatro et al. (2012) on pelitic granulite enclaves from the same area did not report any high-pressure metamorphism. These workers identified biotite dehydration melting to produce metapelitic granulite. Although the textural associations of their pelitic

granulite are similar to those in our study, there are small differences in phase chemical characters. It should be mentioned here that the occurrence of mafic and pelitic granulites having contrasting  $P$ - $T$  histories is not rare in nature (e.g. Faak et al., 2012 from the Sikkim Himalayas). Coexistence of high-pressure metabasic granulite and low-pressure pelitic granulite at the same crustal level implies crustal juxtaposition by the later orogenic process (Faak et al., 2012). The emplacement of  $M_1$  metamorphosed mafic granulite to the mid-crustal level possibly occurred in a subduction-collision type setting dominated by thrusting and shearing which caused juxtaposition of widely different crustal sections. Identification and documentation of such older deep crustal metamorphic event is extremely crucial to understand the lower crustal dynamics in terms of plate tectonics (delamination and/or slab break off) during Archean time.

Correlation of the thrust-related fabric within the intrusive granite and rocks of the Rengali granulite suite near the Sukinda Thrust (with the  $D_{2C}$  event in the cratonic part) clearly implies that a large part of the SC was remobilized and affected by the later  $D_{2M}$  event in the Rengali granulite. This mobilization process extended further north (up to the Dholakmundi Fault in Fig. 2), after which the dominant structural grain within the SC rocks attains a NW–SE orientation from the dominant E–W trend south of the fault. We argue that the swing in structural trend within the SC rocks north and south of the Dholakmundi Fault resulted from the effect of the emplacement of lower to mid-crustal thrust sheet (Rengali granulites). The absence of a strong pervasive later deformation and near-parallel orientation of the map-scale  $F_{1C}$  and  $F_{2C}$  fold axial traces,

**Table 5**  
Whole rock XRF data of mafic and pelitic granulites used for pseudosection analysis.

|                                | RNG 65A | RNG 62b |
|--------------------------------|---------|---------|
| SiO <sub>2</sub>               | 48.033  | 53.555  |
| TiO <sub>2</sub>               | 1.846   | 0.873   |
| Al <sub>2</sub> O <sub>3</sub> | 12.7    | 19.73   |
| FeO <sup>T</sup>               | 16.3    | 15.242  |
| MnO                            | 0.233   | 0.219   |
| MgO                            | 6.211   | 6.646   |
| CaO                            | 10.399  | 1.445   |
| Na <sub>2</sub> O              | 2.162   | 0.952   |
| K <sub>2</sub> O               | 0.203   | 1.312   |
| P <sub>2</sub> O <sub>5</sub>  | 0.16    | 0.043   |
| Total                          | 98.247  | 100.017 |

FeO<sup>T</sup> = Total iron oxide measured.



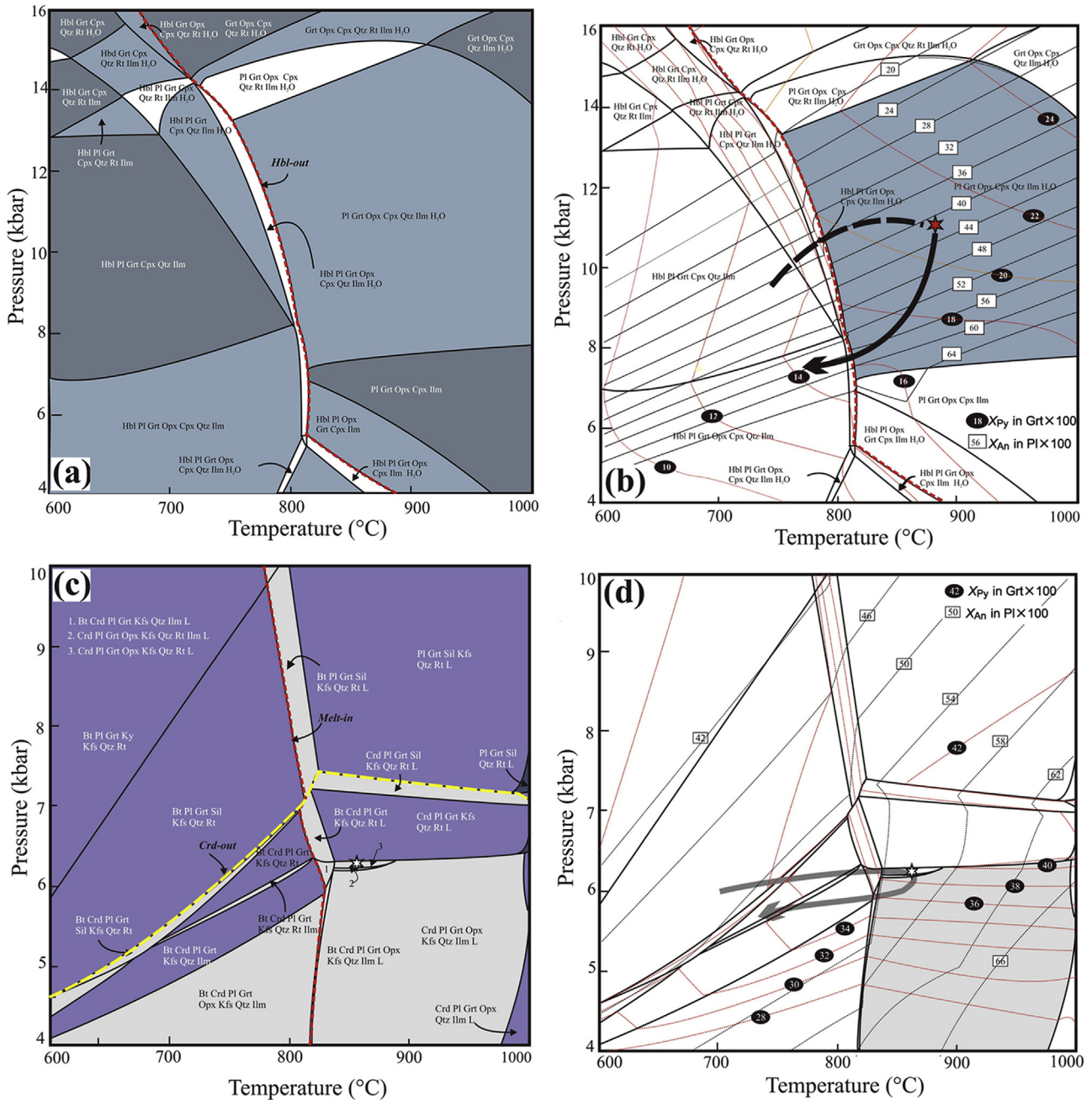


**Figure 8.** *P-T* pseudosections constructed at calculated bulk compositions from representative studied samples to demonstrate *P-T* evolution of mafic (a, b) and pelitic granulite (c, d). Bulk compositions for each were taken from whole rock XRF data presented in Table 5. Each pseudosection is contoured with isopleths of two important mineral compositions; those are  $X_{Py}^{Grt}$  ( $=Mg/(Mg + Fe^{2+} + Mn + Ca)$ ) and  $X_{An}^{Pl}$  ( $=Ca/(Ca + Na + K)$ ). (a) *P-T* pseudosection for the sample RNG 65A constructed in the system  $Na_2O-CaO-FeO-MgO-MnO-Al_2O_3-SiO_2-TiO_2-H_2O$ . Stability fields of different variance are shown in blue and gray shades. The peak  $M_1$  assemblage of Grt-Cpx-Pl-Opx-Qtz-Ilm-L is stable over  $T > 750^\circ C$  at pressure  $> 6.5$  kbar occupying a large *P-T* window. (b) The same section only showing calculated  $X_{Py}$  and  $X_{An}$  isopleths. The position of the  $M_1$  peak is (shown in the asterisk) fixed from the intersection of isopleths showing observed peak mineral compositions. The  $M_{1R}$  path is dominated by development of hornblende-bearing assemblages along a decompressive *P-T* path. (c) *P-T* pseudosection in the system  $K_2O-Na_2O-CaO-FeO-MgO-Al_2O_3-MnO-SiO_2-TiO_2-H_2O$  for the metapelitic granulite sample RNG 62b. The *P-T* window of the peak ( $M_2$ ) metamorphism is shown by the high variance assemblage Grt-Opx-Crd-Pl-Kfs-Qtz-Ilm-L. (d) The same section contoured with calculated  $X_{Py}$  and  $X_{An}$  isopleths. The asterisk represents the approximate position of the peak which is fixed by the intersection respective garnet and plagioclase compositions observed. Note that the peak is achieved by partial melting of biotite-bearing assemblage as deduced from the texture. See text for further details.

the non-cylindricity of the large  $F_{2c}$  folds could also be viewed as a result of this event, a combination of dominant N–S compression coupled with a strong non-coaxial (top-to-the-north shear) deformation. Timing of this thrusting event is yet to be known, but recent geochronological data show that the syn-kinematic granite emplacement within this Rengali granulite occurred at ca. 2.80 Ga (Bose et al., 2013) which closely matches with the dominant monazite Th-U-Pb age from the pelitic granulite (Mahapatro et al.,

2012; Bose et al., 2013). The timing of the  $M_1$  event is still uncertain, but it must be older than 2.80 Ga based on available textural and field relation criteria and limited geochronological data (Bose et al., 2013). During this event, the deep crustal section was incorporated within the mid-crustal level and the entire section was later thrust on top of the cratonic sediments.

It has been proposed recently that the southern part of SC (SIOG) preserves an early history of accretion along an active continental

margin during ca. 3.50–3.10 Ga which gave way to a later development of passive margin characterized by the thick stable shelf arenites (Mukhopadhyay et al., 2012). The development of mature shelf succession on the cratonic block warrants the existence of a major marine basin that might have opened up to the south of the SC during the deposition of the siliciclastics on a passive margin shelf. This is important since a change from an active to passive margin implies cratonization of the former. Structural and metamorphic analyses of the craton margin rocks further suggests that the passive margin deposit along with its cratonized basement of the deformed SIOG rocks were further deformed and remobilized under the impending northerly verging thrust front of the Rengali granulites at ca. 2.80 Ga. The extent of such remobilization is traced for a distance of at least 30 km due north from the Sukinda Thrust. Dominant thrust-related deformation and high-pressure metamorphism along the southern margin of SC possibly implies reestablishment of an accretionary setting which culminated in the final juxtaposition of the two contrasting belts along the Sukinda Thrust. Although this is speculative in absence of quality geochemical and geophysical data, the juxtaposition was responsible for southward growth of SC during the Meso–Neoproterozoic era.

## 6. Conclusions

A narrow strip of granulite belt separating the low-grade rocks of the Archean SC and the high-grade EGMB is identified as the Rengali granulite suite. This belt is composed of charnockite and granite gneiss that host enclaves of mafic and pelitic granulites. Macroscopic and microscopic structures reveal that the Rengali high-grade rocks suffered at least two phases of deformation of which the later phase is shared by the cratonic rocks. Petrological data from the granulite enclave suite suggest an earlier collisional orogeny ( $M_1$ – $D_1$ ) in the Rengali Province caused the burial of the lower crust down to 35–40 km (10–12 kbar, 860 °C) followed by decompression, cooling, and rehydration. Tectonic rejuvenation caused variable-scale partial melting accompanying thrusting and emplacement of synkinematic granitoid. It brought the Rengali high-grade rocks in contact with the low-grade rocks of the SC by thrusting and shearing with a top-to-the-north vergence. This entire evolutionary history further demarcates the southward growth of the Singhbhum Craton during Meso–Neoproterozoic era.

## Acknowledgments

We sincerely thank David Kelsey for inviting us to contribute to this special volume. SB, GG and JM acknowledge financial support from CSIR, India through a major research scheme (No. 24(0312)/10/EMR-II). We also acknowledge UGC-CAS facility and the DST-FIST facility of the Department of Geology, Presidency University. We are thankful to Dr. S.S. Thakur of Wadia Institute of Himalayan Geology, Dehradun and Ms. Aloka Dey of Indian Institute of Technology, Kharagpur during EPMA works. Constructive comments from Pavel Pitra and Sajeev Krishnan improved the quality of the paper. This is a part of the Ph.D. dissertation of SG.

## References

- Anderson, J.L., Smith, D.R., 1995. The effects of temperature and  $fO_2$  on the Al-in-hornblende barometer. *American Mineralogist* 80, 549–559.
- Beard, J.S., Lofgren, G.E., 1991. Dehydration melting and water-saturated melting of basaltic and andesitic greenstones and amphibolites at 1, 3, 6.9 kb. *Journal of Petrology* 32, 365–401.
- Bhattacharya, A., Mohanty, L., Maji, A., Sen, S.K., Raith, M., 1992. Non-ideal mixing in the phlogopite–annite boundary: constraints from experimental data on Mg–Fe partitioning and reformulation of the biotite–garnet geothermometer. *Contributions to Mineralogy and Petrology* 111, 87–93.
- Bhattacharya, A., Krishnakumar, K.R., Raith, M., Sen, S.K., 1991. An improved set of a-X parameters for Fe–Mg–Ca garnets and refinement of the orthopyroxene–garnet–plagioclase–quartz barometer. *Journal of Petrology* 32, 629–656.
- Bishop, F.C., 1980. The distribution of  $Fe^{2+}$  and Mg between coexisting ilmenite and pyroxene with application to geothermometry. *American Journal of Science* 280, 46–77.
- Bose, S., Das, K., Kimura, K., Hayasaka, Y., Hidaka, H., Dasgupta, A., Ghosh, G., Mukhopadhyay, J., 2013. Zircon and monazite geochronology of the granulites and associated gneisses from the Rengali Province, India: growth of the southern margin of the Singhbhum Craton. *AGU Fall Meeting*, V33D-2793.
- Bose, S., Dunkley, D.J., Dasgupta, S., Das, K., Arima, M., 2011. India–Antarctica–Australia–Laurentia connection in the Paleoproterozoic–Mesoproterozoic revisited: evidence from new zircon U–Pb and monazite chemical age data from the Eastern Ghats Belt, India. *Bulletin of the Geological Society of America* 123, 2031–2049.
- Brown, M., 2002. Retrograde processes in migmatites and granulites revisited. *Journal of Metamorphic Geology* 20, 25–40.
- Carrington, D.P., Harley, S.L., 1995. Partial melting and phase relations in high grade metapelites: an experimental petrogenetic grid in the KFMASH system. *Contributions to Mineralogy and Petrology* 120, 270–291.
- Cawood, P.A., 2005. Terra Australis orogen: Rodinia breakup and development of the Pacific and Iapetus margins of Gondwana during the Neoproterozoic and Paleozoic. *Earth Science Reviews* 69, 249–279.
- Cawood, P.A., Kröner, A., Pisarevsky, S., 2006. Precambrian plate tectonics: criteria and evidence. *GSA Today* 1, 4–11.
- Charlier, B., Duchesne, J.-C., Vander Auwera, J., Storme, J.-Y., Maquil, R., Longhi, J., 2010. Polybaric fractional crystallization of high-alumina basalt parental magmas in the Egersund–Ogna Massif-type anorthosite (Rogaland, SW Norway) constrained by plagioclase and high-alumina orthopyroxene megacrysts. *Journal of Petrology* 51, 2515–2546.
- Condie, K.C., 2007. Accretionary orogens in space and time. In: Hatcher Jr., R.D., Carlson, M.P., McBride, J.H., Martínez Catalán, J.R. (Eds.), 4-D Framework of Continental Crust, vol. 200. *GSA Memoir*, pp. 145–158.
- Condie, K.C., Kröner, A., 2008. When did plate tectonics begin? Evidence from the geological record. In: Condie, K.C., Pease, V. (Eds.), *When Did Plate Tectonics Begin?*, vol. 440. *Geological Society of America Memoir*, pp. 281–295.
- Connolly, J.A.D., 2005. Computation of phase equilibria by linear programming: a tool for geodynamic modeling and its application to subduction zone decarbonation. *Earth and Planetary Science Letters* 236, 524–541.
- Connolly, J.A.D., Petrin, K., 2002. An automated strategy for calculation of phase diagram sections and retrieval of rock properties as a function of physical conditions. *Journal of Metamorphic Geology* 20, 697–708.
- Crowe, W.A., Cosca, M.A., Harris, L.B., 2001.  $^{40}Ar/^{39}Ar$  geochronology and Neoproterozoic tectonics along the northern margin of the Eastern Ghats Belt in north Orissa, India. *Precambrian Research* 108, 237–266.
- Crowe, W.A., Nash, C.R., Harris, L.B., Leeming, P.M., Rankin, L.R., 2003. The geology of the Rengali Province: implications for the tectonic development of Northern Orissa, India. *Journal of Asian Earth Sciences* 21, 697–710.
- Dale, J., Powell, R., White, R.W., Elmer, F.L., Holland, T.J.B., 2005. A thermodynamic model for Ca–Na clinopyroxenes in  $Na_2O$ – $CaO$ – $FeO$ – $MgO$ – $Al_2O_3$ – $SiO_2$ – $H_2O$ – $O$  for petrological calculations. *Journal of Metamorphic Geology* 23, 771–791.
- Das, K., Bose, S., Karmakar, S., Dunkley, D.J., Dasgupta, S., 2011. Multiple tectono-metamorphic imprints in the lower crust: first evidence of ca. 950 Ma (zircon U–Pb SHRIMP) compressional reworking of UHT aluminous granulites from the Eastern Ghats Belt, India. *Geological Journal* 46, 217–239.
- Dasgupta, S., Bose, S., Das, K., 2013. Tectonic evolution of the Eastern Ghats Belt. *Precambrian Research* 227, 247–258.
- Dewey, J.F., 2007. The secular evolution of plate tectonics and the continental crust: an outline. In: Hatcher Jr., R.D., Carlson, M.P., McBride, J.H., Catalán, J.M. (Eds.), 4-D framework of continental crust, vol. 200. *Geological Society of America Memoir*, pp. 1–8.
- Dobmeier, C., Raith, M.M., 2003. Proterozoic East Gondwana: supercontinent assembly and breakup. In: Yoshida, M., Windley, B.F., Dasgupta, S. (Eds.), *Proterozoic East Gondwana: supercontinent assembly and breakup*, vol. 206. *Geological Society London Special Publication*, pp. 145–168.
- Dymek, R.F., Gromet, L.P., 1984. Nature and origin of orthopyroxene megacrysts from the St. Urbain anorthositic massif, Quebec. *Canadian Mineralogist* 22, 297–326.
- Emslie, R.F., 1975. Pyroxene megacrysts from anorthositic rocks: a new clue to the sources and evolution of the parent magmas. *Canadian Mineralogist* 13, 138–145.
- Ennih, N., Liégeois, J.-P., 2008. The boundaries of the West African craton, with special reference to the basement of the Moroccan metacratonic Anti-Atlas belt. In: Ennih, N., Liégeois, J.-P. (Eds.), *The boundaries of the West African craton*, vol. 297. *Geological Society London Special Publication*, pp. 1–17.
- Faak, K., Chakraborty, S., Dasgupta, S., 2012. Petrology and tectonic significance of metabasite slivers in the Lesser and Higher Himalayan domains of Sikkim, India. *Journal of Metamorphic Geology* 30, 599–622.
- Fram, M., Longhi, J., 1992. Phase equilibria of dikes associated with Proterozoic anorthosite complexes. *American Mineralogist* 77, 605–616.
- Ganguly, J., 1979. Garnet and clinopyroxene solid solutions and geothermometry based on Fe–Mg distribution coefficient. *Geochimica et Cosmochimica Acta* 43, 1021–1029.

- Ghosh, G., Bose, S., Guha, S., Mukhopadhyay, J., Aich, S., 2010. Remobilization of the southern margin of the Singhbhum Craton, eastern India during the Eastern Ghats orogeny. *Indian Journal of Geology* 80, 97–114.
- Gray, D., Foster, D., 2004. Tectonic evolution of the Lachlan Orogen, southeast Australia: historical review, data synthesis and modern perspectives. *Australian Journal of Earth Sciences* 51, 773–817.
- Gupta, S., 2012. Strain localization, granulite formation and geodynamic setting of 'hot orogens': a case study from the Eastern Ghats Province, India. *Geological Journal* 47, 334–351.
- Harris, N.B.W., Holland, T.J.B., 1984. The significance of cordierite-hypersthene assemblages from the Beitbridge region of the central Limpopo Belt: evidence for rapid decompression in the Archean? *American Mineralogist* 69, 1036–1049.
- Holland, T.J.B., Blundy, J., 1994. Non-deal interactions in calcic amphiboles and their bearing on amphibole-plagioclase thermometry. *Contributions to Mineralogy and Petrology* 116, 433–447.
- Holland, T.J.B., Powell, R., 1998. An internally consistent thermodynamic data set for phases of petrological interest. *Journal of Metamorphic Geology* 16, 309–343.
- Holland, T.J.B., Powell, R., 2003. Activity-composition relations for phases in petrological calculations: an asymmetric multicomponent formulation. *Contributions to Mineralogy and Petrology* 145, 492–501.
- Kar, R., Bhattacharya, S., Sheraton, J.W., 2003. Hornblende dehydration melting in mafic rocks and the link between massif-type charnockite and associated granulites, Eastern Ghats granulite belt, India. *Contributions to Mineralogy and Petrology* 145, 707–729.
- Karlstrom, K.E., Ahall, K.-I., Harlan, S.S., Williams, M.L., McLelland, J., Geissman, J.W., 2001. Long-lived (1.8–1.0 Ga) convergent orogen in southern Laurentia, its extensions to Australia and Baltica, and implications for refining Rodinia. *Precambrian Research* 111, 5–30.
- Kohn, M.J., Spear, F.S., 1989. Empirical calibration of geobarometers for the assemblage garnet + hornblende + plagioclase + quartz. *American Mineralogist* 74, 77–84.
- Korhonen, F.J., Saw, A.K., Clark, C., Brown, M., Bhattacharya, S., 2011. New constraints on UHT metamorphism in the Eastern Ghats Province through the application of phase equilibria modelling and in situ geochronology. *Gondwana Research* 20, 764–781.
- Kretz, R., 1982. Transfer and exchange equilibria in a portion of the pyroxene quadrilateral as deduced from natural and experimental data. *Geochimica et Cosmochimica Acta* 46, 411–422.
- Kröner, A., Hegner, E., Lehmann, B., Heinhorst, J., Wingate, M.T.D., Liu, D.Y., Ermelov, P., 2008. Paleozoic arc magmatism in the Central Asian Orogenic Belt of Kazakhstan: SHRIMP zircon ages and whole-rock Nd isotopic systematics. *Journal of Asian Earth Sciences* 32, 118–130.
- Lee, H.Y., Ganguly, J., 1988. Equilibrium compositions of coexisting garnet and orthopyroxene: experimental determinations in the system FeO-MgO-Al<sub>2</sub>O<sub>3</sub>-SiO<sub>2</sub> and applications. *Journal of Petrology* 29, 93–113.
- Longhi, J., Vander Auwera, J., Fram, M., Monthieth, J.N., 1993. Pressure effects, kinetics and rheology of anorthositic and related magmas. *American Mineralogist* 78, 1016–1030.
- Mahalik, N.K., 1994. Geology of the contact between the Eastern Ghats Belt and North Orissa Craton, India. *Journal of the Geological Society of India* 44, 41–51.
- Mahapatro, S.N., Pant, N.C., Bhowmik, S.K., Tripathy, A.K., Nanda, J.K., 2012. Archean granulite facies metamorphism at the Singhbhum craton-Eastern Ghats Mobile Belt interface: implication for the Ur supercontinent assembly. *Geological Journal* 47, 312–333.
- McCarthy, T.C., Patino Douce, A.E., 1998. Empirical calibration of the silica-Ca-tschermak's-anorthite (SCAn) geobarometer. *Journal of Metamorphic Geology* 16, 675–686.
- Moecher, D.P., Essene, E.J., Anovitz, L.M., 1988. Calculation and application of clinopyroxene-garnet-plagioclase-quartz geobarometers. *Contributions to Mineralogy and Petrology* 100, 92–106.
- Misra, S., 2006. Precambrian chronostratigraphic growth of Singhbhum-Orissa craton, eastern Indian shield; an alternative model. *Journal of the Geological Society of India* 67, 356–378.
- Misra, S., Moitra, S., Bhattacharya, S., Sivaraman, T.V., 2000. Archean granulites at the contact of Eastern Ghats Granulite Belt and Singhbhum-Orissa Craton, in Bhubaneswar-Rengali sector, Orissa, India. *Gondwana Research* 3, 205–213.
- Möller, A., Appel, P., Mezger, K., Schenk, V., 1995. Evidence for a 2 Ga subduction zone: eclogites in the Usagaran belt of Tanzania. *Geology* 23, 1067–1070.
- Mukhopadhyay, D., 2001. The Archean nucleus of Singhbhum: the present state of knowledge. *Gondwana Research* 4, 307–318.
- Mukhopadhyay, J., Ghosh, G., Zimmermann, U., Guha, S., Mukherjee, T., 2012. A 3.51 Ga bimodal volcanics-BIF-ultramafic succession from Singhbhum Craton: implications for Palaeoarchean geodynamic processes from the oldest greenstone succession of the Indian subcontinent. *Geological Journal* 47, 284–311.
- Newton, R.C., Charlu, T.V., Kleppa, O.J., 1980. Thermochemistry of the high structural state plagioclases. *Geochimica et Cosmochimica Acta* 44, 933–941.
- Nichols, G.T., Berry, R.F., Green, D.H., 1992. Internally consistent gahnite-spinel-cordierite-garnet equilibria in the FMASHZn system: geothermobarometry and applications. *Contributions to Mineralogy and Petrology* 111, 362–377.
- O'Brien, P.J., 2008. Challenges in high-pressure granulite metamorphism in the era of pseudosections: reaction textures, compositional zoning and tectonic interpretation with examples from the Bohemian Massif. *Journal of Metamorphic Geology* 26, 235–251.
- Owens, B.E., Dymek, R.F., 1995. Significance of pyroxene megacrysts for massif anorthosite petrogenesis: constraints from the Labrieville, Quebec, pluton. *American Mineralogist* 80, 144–161.
- Pattison, D.R.M., 2003. Petrogenetic significance of orthopyroxene-free garnet-clinopyroxene-plagioclase ± quartz-bearing metabasites with respect to the amphibolite and granulite facies. *Journal of Metamorphic Geology* 21, 21–34.
- Pattison, D.R.M., Chacko, T., Farquhar, J., McFarlane, C.R.M., 2003. Temperatures of granulite facies metamorphism: constraints from experimental phase equilibria and thermometry corrected for retrograde exchange. *Journal of Petrology* 44, 867–900.
- Pitra, P., Kouamelan, N., Ballèvre, M., Peucat, J.-J., 2010. Palaeoproterozoic high-pressure granulite overprint of the Archean continental crust: evidence for homogeneous crustal thickening (Man Rise, Ivory Coast). *Journal of Metamorphic Geology* 28, 41–58.
- Polat, A., Appel, P.W.U., Brian, F.J., 2011. An overview of the geochemistry of Eoarchean to Mesarchean ultramafic to mafic volcanic rocks, SW Greenland: implications for mantle depletion and petrogenetic processes at subduction zones in the early Earth. *Gondwana Research* 20, 255–283.
- Pownceby, M.I., Wall, V.J., O'Neill, H.St.C., 1987. Fe-Mn partitioning between garnet and ilmenite: experiments and applications. *Contributions to Mineralogy and Petrology* 97, 116–126.
- Racek, M., Stipská, P., Powell, R., 2008. Garnet-clinopyroxene intermediate granulites in the St. Leonhard massif of the Bohemian Massif: ultrahigh-temperature metamorphism at high pressure or not? *Journal of Metamorphic Geology* 26, 253–271.
- Ravna, E.K., 2000. Distribution of Fe<sup>2+</sup> and Mg between coexisting garnet and hornblende in synthetic and natural systems: an empirical calibration of the garnet-hornblende Fe-Mg geothermometer. *Lithos* 53, 265–277.
- Rushmer, T., 1993. Experimental high pressure granulites: some application to natural mafic xenolith suites and Archaean granulite terranes. *Geology* 21, 411–414.
- Rushmer, T., 1991. Partial melting of two amphibolites: contrasting experimental results under fluid absent conditions. *Contributions to Mineralogy and Petrology* 107, 41–59.
- Saha, A.K., 1994. Crustal evolution of Singhbhum-North Orissa, India. *Memoir Geological Society of India* 27, 341.
- Samuel, V.O., Santosh, M., Liu, S., Sajeev, K., 2014. Neoproterozoic continental growth through arc magmatism in the Nilgiri Block, southern India. *Precambrian Research* 245, 146–173.
- Sawyer, E.W., 1999. Criteria for the recognition of partial melting. *Physics and Chemistry of the Earth* 24, 269–279.
- Schmidt, M.W., 1992. Amphibole composition in tonalite as a function of pressure: an experimental calibration of the Al-in-hornblende barometer. *Contributions to Mineralogy and Petrology* 110, 304–310.
- Skjerlie, K.P., Patinö Douce, A.E., 1995. Anatexis of interlayered amphibolite and pelite at 10 kbar: effect of diffusion of major components on phase relations and melt fraction. *Contributions to Mineralogy and Petrology* 122, 62–78.
- Smithies, R.H., Van Kranendonk, M.J., Champion, D.C., 2007. The Mesoproterozoic emergence of modern-style subduction. *Gondwana Research* 11, 50–68.
- Springer, W., Seck, H.A., 1997. Partial fusion of basic granulites at 5 to 15 kbar: implications for the origin of TTG magmas. *Contributions to Mineralogy and Petrology* 127, 30–45.
- St-Onge, M.R., van Gool, J.A.M., Garde, A.A., Scott, D.J., 2009. Correlation of Archean and Paleoproterozoic units between northeastern Canada and western Greenland: constraining the pre-collisional upper plate accretionary history of the Trans-Hudson orogen. In: Cawood, P.A., Kröner, A. (Eds.), *Earth Accretionary Systems in Space and Time*, vol. 318. Geological Society of London Special Publication, pp. 193–235.
- Stern, R.J., 2005. Evidence from ophiolites, blueschists and ultrahigh-pressure metamorphic terranes that the modern episode of subduction tectonics began in Neoproterozoic time. *Geology* 33, 557–560.
- Vielzeuf, D., Schmidt, M.W., 2001. Melting relations in hydrous systems revisited: application to metapelites, metagreywackes and metabasalts. *Contributions to Mineralogy and Petrology* 141, 251–267.
- Windle, B.F., Garde, A.A., 2009. Arc-generated blocks with crustal sections in the North Atlantic craton of West Greenland: new mechanism of crustal growth in the Archean with modern analogues. *Earth Science Reviews* 93, 1–30.
- Wolf, M.B., Wyllie, P.J., 1994. Dehydration-melting of amphibolite at 10 kbar: the effects of temperature and time. *Contributions to Mineralogy and Petrology* 115, 369–383.